

Inverted time-of-flight backscattering instrument MARS

by Peter Allenspach, Laboratory for Neutron Scattering, ETH Zurich & PSI
Villigen, 5232 Villigen PSI, Switzerland.

(February 2000)

<u>Content:</u>	<u>page</u>
1. Introduction	2
Literature	4
List of abbreviations	5
2. Scientific Case	6
2.1 Present Situation	6
2.2 Outlook	7
2.3 Interest from Swiss research groups	7
2.4 Interest from international research groups	8
3. Dimensioning	9
3.1 Principal layout	9
3.2 Inelastic and frame overlap	11
3.3 Length of primary flight path	14
3.4 Snail and rabbit chopper	19
3.5 Energy resolution in the primary instrument	25
4. Energy analysis	26
4.1 Principal layout	26
4.2 Secondary energy resolution	26
4.3 Mobile analyzer banks	33
5. Instrument data	36
5.1 Energy resolution and energy window	36
5.2 Q-ranges	37
5.3 Intensity	38
5.4 Polarization analysis	42
5.5 Diffraction	42
5.6 Costs	44
5. Conclusion	44

1. Introduction

This report is based on a previous study (891/AP33-701.-). Some details have been updated and a scientific justification has been added.

The aim of this study is to present the design of an inelastic neutron instrument with an energy resolution of up to $1 \mu\text{eV}$ at SINQ. For such a resolution backscattering instruments are best suited (lying in between triple-axis or time-of-flight (TOF) instruments with a maximum resolution of typically $10 \mu\text{eV}$ and spin-echo instruments with resolutions in the neV range). Two different types of backscattering instruments have been built in the past: Conventional backscattering instruments (BS) with monochromator crystals and analyzer crystals both in backscattering position (e.g. IN10 and IN16 at ILL, France) and inverted geometry TOF backscattering instruments (ITOF) with the TOF unit in the primary instrument and analyzer crystals in backscattering position in the secondary instrument (IRIS and OSIRIS at ISIS, UK, and LAM-80 at Tsukuba, Japan).

The first decision which influences the instrument design is the choice of accessible momentum transfer Q . If high Q -values are envisaged high incident and high analyzer energies are needed. Since the energy resolution in the primary instrument of an ITOF is inverse proportional to the time a neutron needs to fly from the first chopper to the sample, for high incident energies and given resolution the primary flight path becomes extremely long (for $1 \mu\text{eV}$ resolution and 2 meV incident energy [corresponding to Si111]: $> 60 \text{ m}$). Hence, for large- Q research a BS is the instrument of choice. For low- Q research both instrument types are feasible from the point of resolution.

If the planned instrument will exclusively be used for quasi elastic or slightly inelastic investigations (up to 0.8 meV energy transfer) an IN10-type instrument equipped with fourteen different monochromators can perform this task. But for investigations far into the inelastic regime (10 meV energy transfer) and for full flexibility in choosing the incident energy an ITOF, where the incident energy is varied by a mere change of chopper phases, is needed.

Since scientific background and interest of the Swiss neutron community lies more in the field of small- Q research (magnetism) and inelastic excitations, the scientific commission of SINQ has decided in June

1995 to favour an ITOF instrument. Other reasons for such an instrument was its higher flexibility and the larger demand (IRIS at ISIS is notoriously overbooked) compared to conventional backscattering machines.

At SINQ the energy resolution for powder samples ranges up to 30 μeV (at the elastic peak position) on the TOF instrument FOCUS, therefore there is no reason to cover the same resolution range with a backscattering instrument with pyrolytic graphite (PG) analyzers as partially done for the IRIS spectrometer. (OSIRIS is exclusively equipped with PG analyzers and designed for polarization analysis). We will solely use mica analyzers (one side of IRIS is equipped with mica analyzers) making a costly analyzer cooling unnecessary. The lower reflectivity of mica compared to graphite (mica 006: 40 % of PG 002) can partially be compensated by equipping both sides of the instrument with mica analyzers (see Chapter 3).

The advantage of a TOF instrument at a pulsed source is obviously the concentration of all neutrons in the pulse used by the instrument. The disadvantages are the fixed values for the pulse duration and the repetition rate. At a steady state source only a tiny fraction of the neutrons can be used when chopping the beam in order to produce a pulse, but pulse duration and repetition rate can freely be chosen by adjusting chopper speed and window.

The instrument presented here (**MARS**: mica analyzer high resolution inverted time-of-flight backscattering spectrometer) was designed under following conditions:

- best energy resolution at the elastic peak: 1 μeV
- high intensity
- largest possible energy window which is easy to shift in energy
- separation of the different analyzer reflections (002, 004, 006, 008)
- diffraction option
- most parts (choppers, detectors, etc.) commercially available

The resulting instrument is an inverted TOF machine with five choppers running with 50 Hz (up to 350 Hz for the first chopper) and a secondary instrument with movable banks of mica analyzers on both sides of the instrument. A total length of the primary instrument of 38.6 m and a diameter of 3 m (without shielding) for the secondary instrument.

(see also: http://www1.psi.ch/www_sinq_hn/SINQ/instr/MARS.html)

Literature used for this study:

"A dynamic range upgrade for neutron backscattering spectroscopy"
J. C. Cook, W. Petry, A. Heidemann, and J - F. Barthélemy, Nuclear Instruments and Methods in Physics Research **A312**, (1992) 553-560.

"The design of the IRIS inelastic neutron spectrometer and improvements to its analysers"
C. J. Carlile and M. A. Adams, Physica B **182**, (1992) 431-440.

"Neutronenspektrometer mit μeV -Auflösung unter Benutzung von Flugzeit- und Rückstreumethoden"
A. Heidemann and G. Jenkin, Internal Report 80HE01S, ILL Grenoble, France.

"A high-resolution inverted time-of-flight spectrometer for reactor cold-sources"
G. J. Kearley and F. Trouw, Journal of Neutron Research **1** (3), (1993) 45-51.

"The OSIRIS polarisation analysis spectrometer and diffractometer"
D. Martin, S. Campbell, and C. J. Carlile, J. Phys. Soc. Jpn **65**, (1996) Suppl. A pp. 245-248.

List of abbreviations and instrument parameters:

α	:	beam divergency (rad)
α_B	:	angle defined by the beam width and the chopper radius ($^\circ$)
α_{ch}	:	aperture of chopper window ($^\circ$)
α_p	:	$= \alpha_B + \alpha_{ch}$ ($^\circ$)
η	:	mosaic spread (rad)
λ_i	:	mean incident wavelength (\AA)
$\delta\lambda$:	wavelength uncertainty [FWHM] (\AA)
Θ	:	scattering angle (rad)
$\delta\Theta$:	scattering angle uncertainty [FWHM] (rad)
D	:	sample-detector distance (m)
d_B	:	horizontal beam width (m)
d_{00L}	:	lattice spacing of mica reflection 00L (\AA)
E_i	:	mean incident energy (meV)
E_{00L}	:	energy of analyzer reflection 00L (meV)
δE	:	energy uncertainty [FWHM] (meV)
δE_{prim}	:	energy uncertainty of primary instrument [FWHM] (meV)
δE_{sec}	:	energy uncertainty of secondary instrument [FWHM] (meV)
ΔE_{00L}	:	energy window for analyzer reflection 00L (meV)
f	:	chopper frequency (Hz)
k	:	mean incident wave vector (\AA^{-1})
δk	:	wave vector uncertainty [FWHM] (\AA^{-1})
L	:	chopper 1 - sample distance (m)
l_{ij}	:	distance from chopper i to chopper j (m)
r_B	:	chopper radius from center to bottom of beam (m)
t	:	chopper 1 to sample flight time of a neutron with energy E_i (s)
t_{00L}	:	sample to detector flight time of a neutron with the 00L-analyzer energy (s)
δt	:	time uncertainty [FWHM] (s)
Δt	:	time window at sample (s)
Δt_{00L}	:	time window at sample for analyzer reflection 00L (s)
v	:	mean speed of incident neutrons (m/s)
δv	:	neutron speed uncertainty (m/s)
v_{00L}	:	neutron speed for analyzer reflection 00L (m/s)

The remaining variables appearing in the text are defined in the corresponding figures.

2. Scientific Case

2.1 Present Situation

The need for an instrument like MARS can be judged from the demand for IRIS and OSIRIS. IRIS, running now for 15 years, has during this time decisively contributed in many fields of research:

Translational and rotational diffusion

- Polymers - Measurement of polymer mobility around T_g , segmental motion, CH_3 side-group rotation, polymer blends, conducting polymers
- Liquids - molten alloys (high ionic conductivity), aqueous solutions (electrolytes), colloidal systems
- Zeolites (catalysts) + benzene, methanol etc
- Water in biological systems
- Metal hydrides - mobile phone batteries
- Protonic conductors (ceramics)

Magnetic excitations

- Crystal field transitions (High- T_c , CMR, Perovskites)
- Low-dimensional systems
- Anomalous spin diffusion in low-dimensional systems (fractal behavior)

Excitations in quantum fluids

- Helium-4, Helium-3/Helium-4 mixtures
- Hydrogen
- Helium and hydrogen in confinement (aerogels, vycor)

Tunnelling spectroscopy

- Small molecules on surfaces (used as probe)
- Rare gas matrices (free rotors)
- Intercalates
- Molecular systems (rotor used as probe of the molecular environment)

The huge success of IRIS has at ISIS initiated the build-up of OSIRIS which is dedicated to **polarization investigations**:

- Structures with unit cells up to 10000 \AA^3 (deuteration of sample not necessary)
- Complicated incommensurate magnetic structures
- Low-energy magnetic excitations in ferromagnets (new materials for the information and telecommunication technology)
- Separation of transverse and longitudinal magnetic excitations (e.g. in strongly correlated electron systems)

- Model-independent determination of coherent and incoherent contributions in polymers, glasses and liquids

All these topics will be covered by MARS as well, but its uncontaminated analyzer reflections, its ultra-high inelastic resolution, and its resolution adaption will yield an unprecedentedly pure and wide dynamic range with μeV resolution.

2.2 Outlook

Following additional problems will be addressed by MARS:

- For soft condensed matter and especially biological research dynamic investigations are up to now still limited to very simple model systems. High quality, high resolution data in a wide energy range and polarization analysis will initiate a step further towards the understanding of the dynamics of more realistic systems.
- The observation and understanding of quantum tunneling effects in artificially designed molecular magnets is vital for a development of quantum computers and data storage on a molecular scale. Such research is still hampered by the limited energy range of high resolution spectroscopy.
- Magnetic excitations of metal ions in metalloproteins (such as chlorophyll or haemoglobin) will yield direct insight into the dynamics of these operational units of life.
- Spectroscopic transitions and their strength define the underlying states, while the widths of transitions depend on the life-time of these states. This very valuable additional information (as a function of system parameters such as temperature, magnetic field or pressure) is normally very hard to obtain, since very often the intrinsic line-widths are smaller than the instrumental resolution. MARS offers here unprecedented capabilities to measure line widths of excitations in the meV range with μeV resolution.

2.3 Interest from Swiss research groups (projects supported by the Swiss National Science Foundation)

- Prof. H.U. Güdel, Univ. Bern: Magnetic interaction in molecular transition-metal compounds.
- Prof. K. Yvon, Univ. de Genève: Hydrogen diffusion in metal hydrides.
- Prof. L. Schlapbach, Univ. de Fribourg: Hydrogen diffusion in metal clusters.

- Prof. P. Schurtenberger, Univ. de Fribourg: Dynamics of strongly interacting colloidal suspensions.
- LNS: low-energy excitations and crystal-field transitions (high-T_c compounds, Kondo systems, heavy electron systems).

2.4 Interest from international research groups

Many neutron users have expressed their wish for instruments with higher energy resolution than presently available at SINQ or other neutron sources. In the past - due to a lack of specific inelastic instruments - quasielastic investigations were the realm of high resolution spectroscopy. The demand for quasielastic instruments is still very high and satisfied by many instruments world-wide. But today's hot topics in science more and more ask for high resolution inelastic investigations (see above) for which the international suite of instruments is insufficient. MARS with its versatile design will open here new possibilities for uncontaminated μeV -resolution inelastic investigations.

3. Dimensioning

3.1 Principal layout

The principal layout of an inverted TOF instrument is shown in Fig. 1. At the first chopper (or at a pulsed source in the source) a pulse of neutrons is created. In a direct TOF instrument the aim is now to cut the desired energy out of the pulse spectrum (i.e. to monochromatize the pulse in the primary instrument). The secondary instrument (after scattering at the sample) is then the TOF part where the energy changes due to inelastic scattering are detected. For the inverted geometry the primary flight path is used to tailor the pulse spectrum into a relatively narrow band of energies by placing at least one additional chopper into the beam.

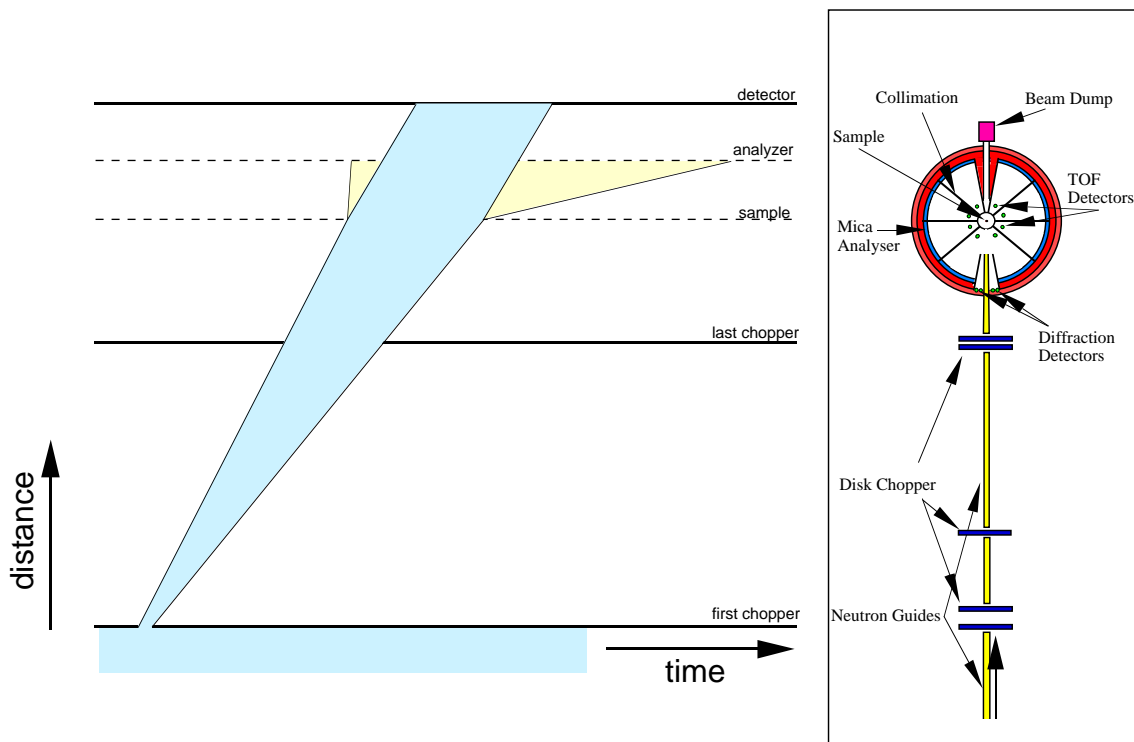


Fig. 1: Principle of an inverted TOF instrument shown in a distance-time (d-t) diagram (left) and the actual design (right).

In practice several choppers are needed in order to suppress slow and fast neutrons originating from earlier and later pulses, respectively (pulse contamination, see Fig. 2). At the sample the fastest neutrons (with highest energy) of the tailored pulse arrive first followed by successively slower

neutrons. On arrival the neutrons are scattered elastically and inelastically. A part of the scattered neutrons hit then the analyzer crystals positioned at a certain distance in backscattering geometry (for high resolution, see Chapter 3). Only neutrons which fulfil Bragg's law for backscattering $\lambda = 2 \cdot d$ (i.e. having the proper wave length or energy) are reflected, while all the others are absorbed or transmitted. (In reality for an inverted TOF instrument a geometry slightly off-backscattering is used. The reason for this will be explained in Chapter 3.) This means that only neutrons (in the primary band) with exactly the energy corresponding to the analyzer and scattered elastically at the sample will be reflected at the analyzer. All the other neutrons in the primary pulse either have to loose or to gain energy during scattering at the sample in order to obtain the appropriate analyzer energy. The neutrons scattered back from the analyzer are then finally counted in a time sensitive detector.

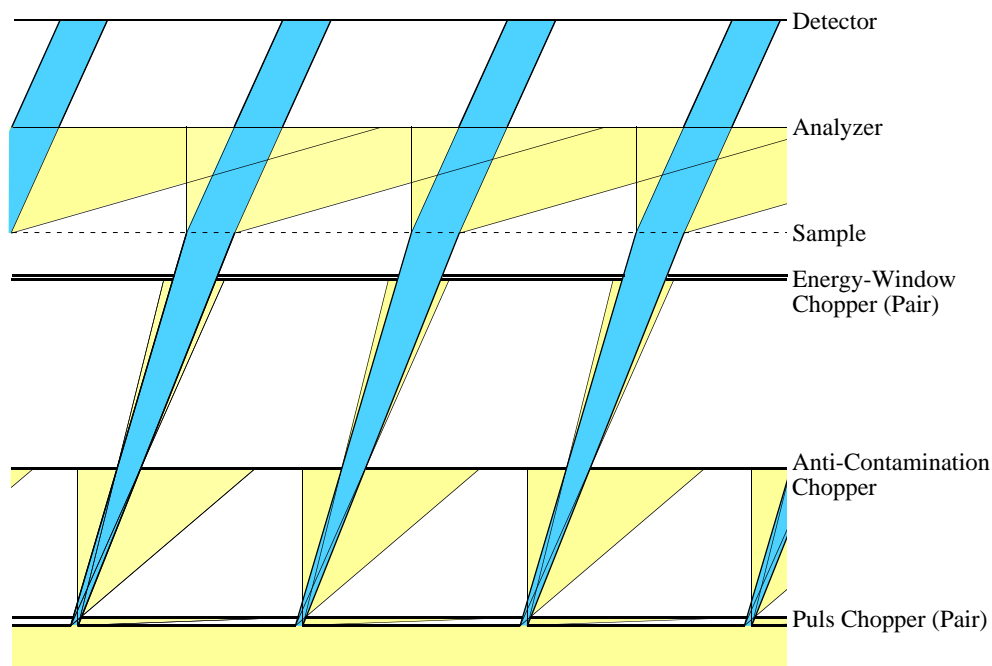


Fig. 2: d-t diagram of an actual instrument.

3.2 Inelastic and frame overlap

A problem now arises from the fact that not only one wave length is reflected from the analyzer but all the higher orders as well (for mica 002 the reflections 004, 006, 008, 0010, and so on). This leads to inelastic overlap shown in Fig. 3 as hatched area. In this regime there is no way to distinguish between neutrons scattered from the 002 or 004 reflection, and therefore the corresponding energy information is lost. In order to solve this problem the detector has to be placed at a large enough distance (depending on Δt) from the sample where no inelastic overlap occurs. In practice a reasonable choice of this distance D will define a time window Δt at the sample which in turn will define the maximum energy window.

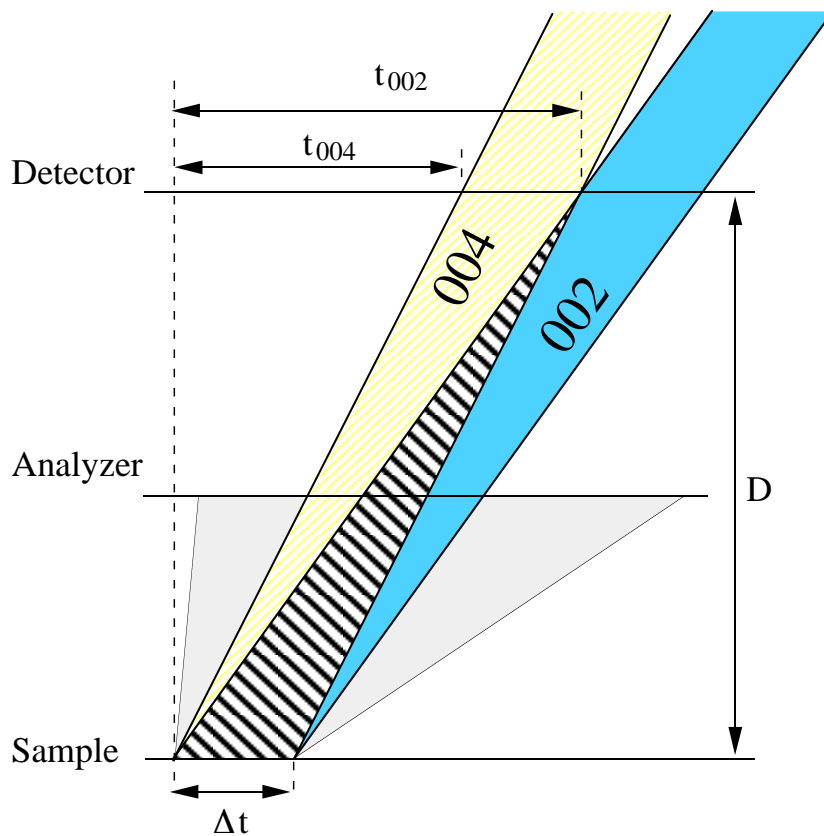


Fig. 3: d-t diagram of the secondary flight path. A pure 002 pulse can be detected when the detector does not intersect the hatched area.

The maximum Δt for a given minimal distance D is given by:

$$\Delta t = \frac{D}{v_{002}} - \frac{D}{v_{004}} = \frac{D}{2 \cdot v_{002}}, \quad (2.1)$$

since:

$$t_{00L} = \frac{D}{v_{00L}}, \text{ and } v_{004} = 2 \cdot v_{002}.$$

(For mica: $v_{002} \approx 200$ m/s.)

By successively reducing Δt (for a fixed D) higher order reflections can be resolved as well (see Fig. 4). With a beryllium filter between sample and analyzer all the reflections higher than 008 are suppressed.

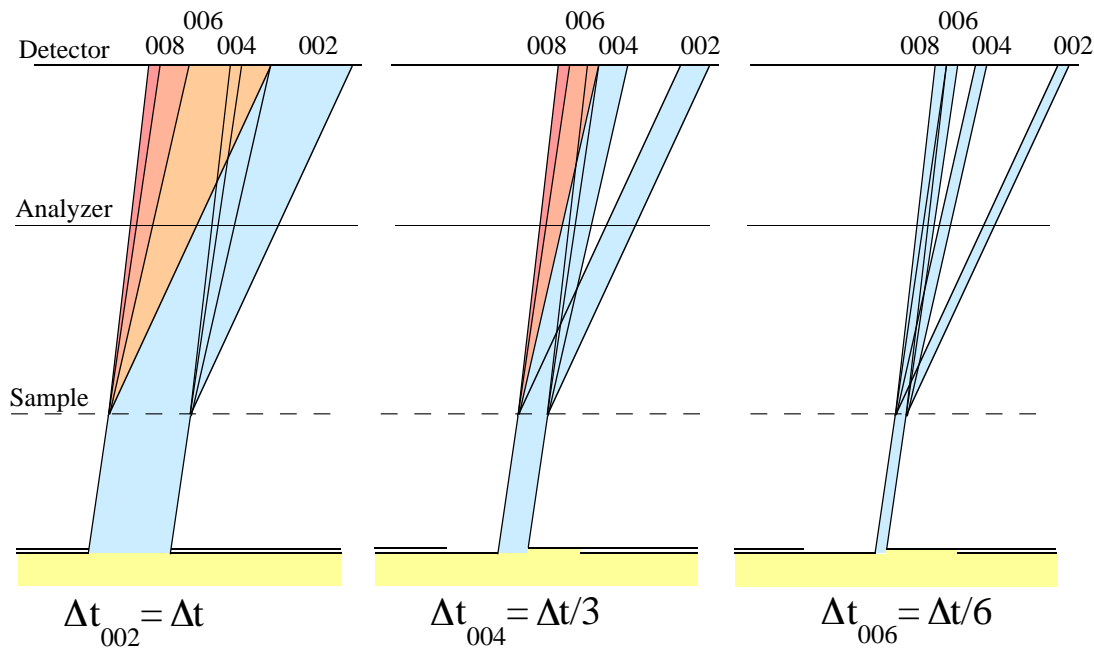


Fig. 4: d-t diagram of the three different time window arrangements. The time windows are adjusted by shifting the relative phase between the last pair of choppers (energy window choppers).

The advantages of four different analyzer energies are: larger accessible Q-range, different energy resolutions, and different energy windows.

For a measurement the results of many different pulses will be added together in order to obtain reasonable statistics. Therefore, a temporal overlap of two successive pulses (frame overlap) has to be avoided (Fig. 5).

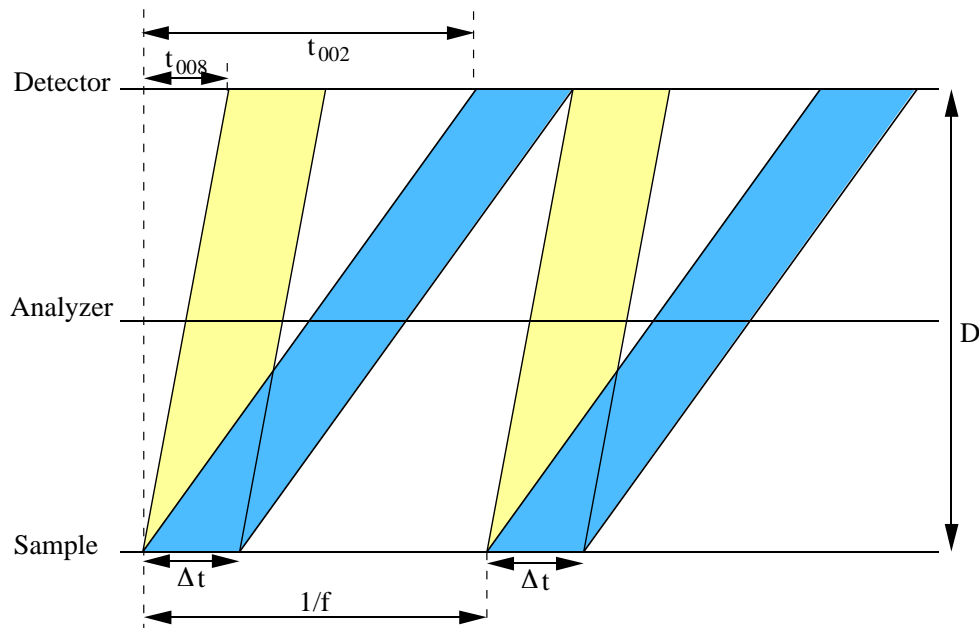


Fig. 5: d-t diagram of two successive neutron pulses (004 and 006 not shown). A higher frequency would result in frame overlap while a lower frequency would waste neutrons.

Frame overlap just starts if:

$$t_{002} + \Delta t = \frac{1}{f} + t_{008}. \quad (2.2)$$

With eq. 2.1 and

$$t_{008} = \frac{t_{002}}{4}, \quad t_{002} = \frac{D}{v_{002}}$$

the maximum chopper frequency turns out to be:

$$f = \frac{4}{5} \cdot \frac{v_{002}}{D}. \quad (2.3)$$

Fig. 6: Frequency f and time window Δt as a function of the length D of the secondary flight path.

3.3 Length of primary flight path

For time-of-flight instruments (TOF) the relative energy resolution $\delta E/E_i$ is depending on the pulse duration δt and the time t the neutrons need to reach the sample:

$$\frac{\delta E_{prim}}{E_i} = 2 \frac{\delta t}{t}. \quad (2.4)$$

The flight time t is given by the distance L between the pulse-producing chopper and the sample as well as the average speed v of the neutrons:

$$t = \frac{L}{v} = \frac{L}{1000 \cdot \sqrt{\frac{E_i}{5.227}}}. \quad (2.5)$$

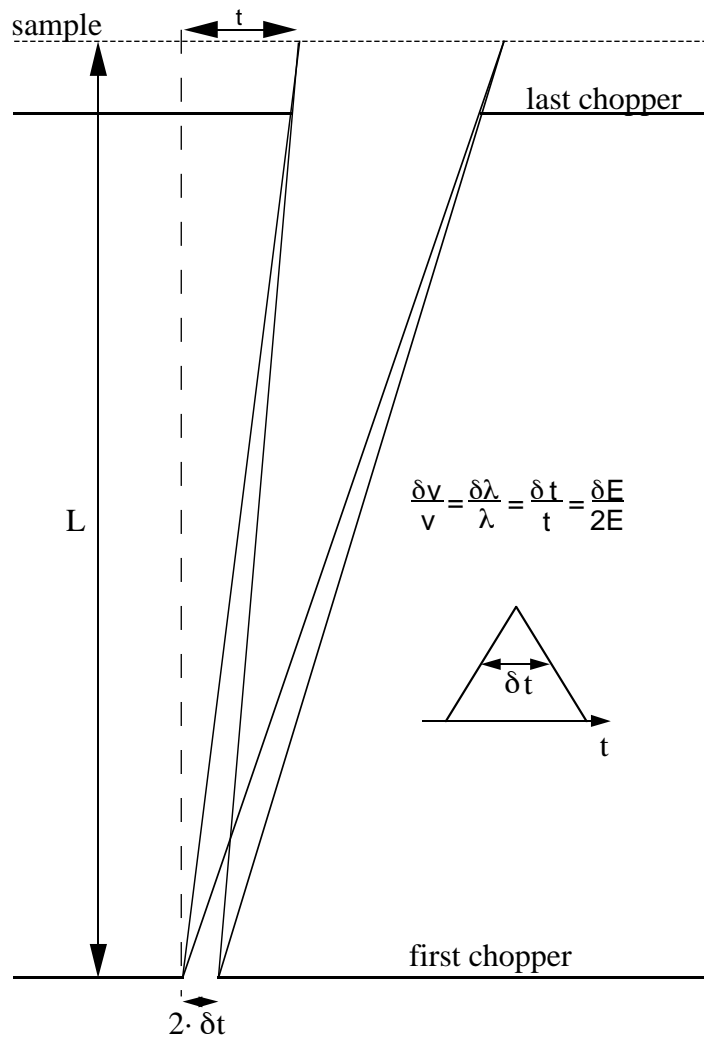


Fig. 7: d-t diagram of the primary flight path indicating the speed (energy) uncertainty of neutron hitting the sample at the same time.

Therefore the pulse width is given by:

$$\delta t = \frac{t \cdot \delta E_{prim}}{2E_i} = \frac{L \cdot \delta E_{prim}}{2000 \cdot \sqrt{\frac{E_i^3}{5.227}}} = 1.1143 \cdot 10^{-3} \frac{L \cdot \delta E_{prim}}{\sqrt{E_i^3}}. \quad (2.6)$$

A neutron pulse with the width δt (FWHM) - assuming a triangular shape - is generated by a disk chopper with the rotation frequency f_{ch} and an opening angle α_p :

$$\delta t = \frac{1}{2} \cdot \frac{1}{f} \cdot \frac{\alpha_p}{360}. \quad (2.7)$$

Since the neutron beam has a finite width d_B , α_p is the sum of the chopper window α_{ch} and the angle α_B defined by the beam width and the chopper radius r_B :

$$\alpha_p = \alpha_{ch} + \alpha_B = \alpha_{ch} + 2 \cdot \arctan\left(\frac{d_B}{2r_B}\right). \quad (2.8)$$

For a single disk chopper we choose $\alpha_{ch} = \alpha_B$. Hence:

$$\alpha_p = 4 \cdot \arctan\left(\frac{d_B}{2r_B}\right). \quad (2.9)$$

Inserting eq. 2.9 into eq. 2.7 and substituting the frequency f by the relation given in eq. 2.3 the resulting pulse duration turns out to be:

$$\delta t = \frac{D \cdot \arctan\left(\frac{d_B}{2r_B}\right)}{144 \cdot v_{002}}. \quad (2.9)$$

Setting eq. 2.9 equal to eq. 2.6 the total distance between first chopper and sample adds up to:

$$L = \frac{125 \cdot D \cdot \sqrt{E_i^3} \cdot \arctan\left(\frac{d_B}{2r_B}\right)}{9 \cdot \sqrt{5.227} \cdot v_{002} \cdot \delta E_{prim}}. \quad (2.10)$$

In order to fix the length of the instrument a primary energy resolution δE_{prim} at the elastic peak position for the 002 reflection ($E_i = E_{002}$) has to be chosen. Eq. 2.10 transforms then into:

$$L = \frac{1}{72} \cdot \frac{E_{002}}{\delta E_{prim}} \cdot D \cdot \arctan\left(\frac{d_B}{2r_B}\right). \quad (2.11)$$

Fig. 8: Chopper frequency and length of primary path as functions of the sample-detector distance for some typical values of chopper dimensions and energy resolution (d_b will in reality only be 1.5 cm due to a converging guide towards the first chopper pair).

Realistically the maximum speed for all five choppers should not exceed much more than 150 Hz (due to prohibitive costs increases with increasing speed). Commercially available choppers (Dornier) of 70 cm diameter and a maximum frequency of 167 Hz (10000 rpm) would define the dimensions of the instrument as displayed in Fig. 8 (chopper radius = $r_B + h_B$).

As can be seen from eqs. 2.1 and 2.11 both the time window Δt and the primary path length L depend linearly on the secondary flight path D , hence the energy window for a given incident energy can only be changed by the variation of the chopper dimensions and the energy resolution (or of course by suppressing some of the pulses).

With the values given in Fig. 8 essentially three different instrument dimensions seem to be feasible for SINQ (Fig. 9):

- (a) $D = 1.1$ m, $L = 12.9$ m, and $f = 150$ Hz
- (b) $D = 2.1$ m, $L = 25.7$ m, and $f = 100$ Hz
- (c) $D = 3.2$ m, $L = 38.6$ m, and $f = 50$ Hz

Option (a) would result in a very compact instrument with short primary and secondary flight paths but with some severe drawbacks:

- Only one side of the instrument could be built due to the close proximity to SANS, resulting in an intensity penalty of a factor two.
- Cramped instrument with only small sample and very small detectors (not available commercially). No room for electronics and sufficient shielding.
- "Fixed" primary energy resolution: $0.707 \mu\text{eV}$ for $E_i = 0.208 \text{ meV}$ and $236 \mu\text{eV}$ for $E_i = 10 \text{ meV}$ (since frequency of first chopper can not be increased to much higher values).
- Due to the small sample size the beam had to be reduced from 12 cm height to 1 cm at the sample position.

For **option (b)** the space and the compression of the beam (factor two to three) remain a problem and on the outside the available room is still severely limited due to SANS (intensity penalty is a factor of two).

Option (c): Very spacious secondary instrument. Large sample (3 cm; beam compression factor = 4). Primary energy resolution can be increased by a factor of seven by running the first chopper on seven times the nominal frequency. Long primary flight path, instrument outside the neutron guide hall.

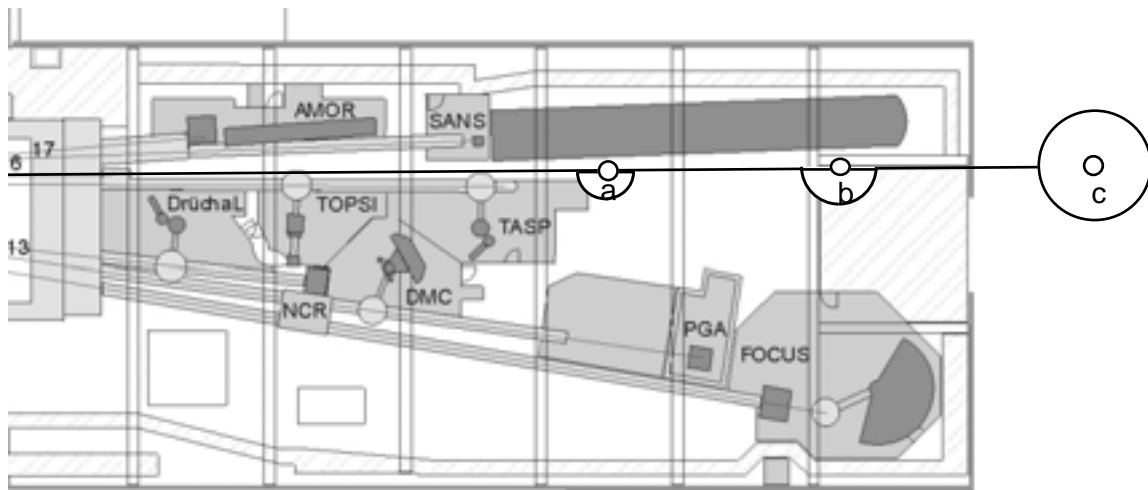


Fig. 9: SINQ neutron guide hall with the three options of an instrument at neutron guide 1RNR15. The last few meters of the supermirror coated guide will consist of a horizontally and vertically converging ($m=3$) anti-trumpet in order to focus the beam onto the sample.

In conclusion: Option (a) is technically not feasible without major PSI-internal development in electronics and detector miniaturization (with uncertain outcome) and would include a severe penalty in intensity and primary resolution. **Option (b)** would certainly be technically less demanding on the side of developments in electronics and detectors, nevertheless no commercially available preamplifiers and detectors could be used and the penalty of resolution and intensity are comparable to option (a). Option (a) and (b) would both produce a very high and intolerable neutron and X-ray background in the vicinity of the SANS-detector which could - due to the space limitations - not be shielded properly. **Option (c)** is the only realistic solution which could be realized with commercially available parts without sacrificing intensity or resolution. The only drawback is the need for an extension of the neutron guide hall.

3.4 Snail and rabbit chopper

Choppers 2 and 3 are designed to block neutrons with energies outside the wished energy window from reaching the sample (Fig. 10). The snail chopper will absorb all neutrons with energies smaller than the useful energy window, but since it has to open for the next pulse after a certain time (roughly $1/f$) there will be a threshold energy below which neutrons will pass anyhow. The aim is now to put this threshold to a value where the neutron flux is already very small. In addition, the possibility in options (b) and (c) to run the choppers with up to seven times the nominal frequency will aggravate this situation (Fig. 11).

The following calculations will yield the chopper distance l_{12} as a function of the threshold energy E_{s1} (corresponding to the speed v_{s1}). The distance l_{12} as a function of E_{s2} and E_{s3} are calculated accordingly. v_a ($= L/t$) in Fig. 11 is the average speed and corresponds to the energy E_j . Neutrons following the time line v_{11} reach the sample at a time $t-\Delta t/2$ but pass chopper 1 earlier by δt than neutrons following v_a . Therefore:

$$v_{11} = \frac{L}{t - \frac{1}{2}\Delta t + \delta t} = \frac{l_{12}}{t_{11}^{12}} \quad (2.12)$$

and

$$v_{s1} = \frac{l_{12}}{\frac{1}{f} - 2 \cdot \delta t + t_{12}^{11}} \quad (2.13)$$

will finally lead with $f_{eff} = n \cdot f$ to:

$$l_{12} = \frac{1}{n} \cdot \frac{\frac{1}{f} - 2 \cdot \delta t}{\frac{1}{v_{sn}} - \frac{1}{v_{1n}}} \quad (2.12)$$

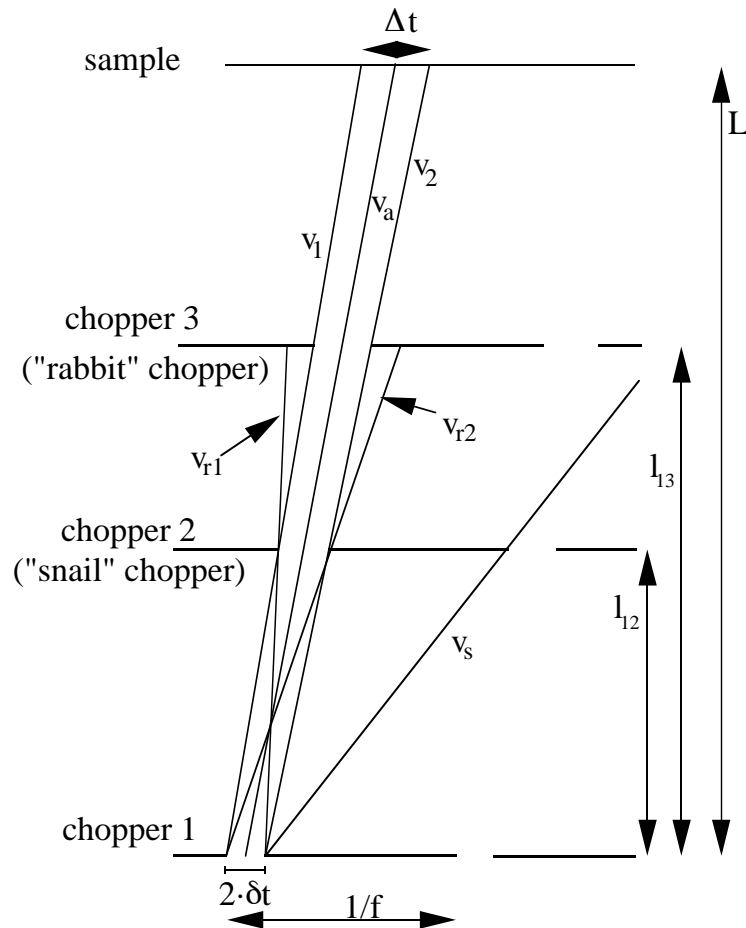


Fig. 10: Schematic d-t diagram of the pulse producing chopper (chopper 1), the snail chopper (2) and the rabbit chopper (3).

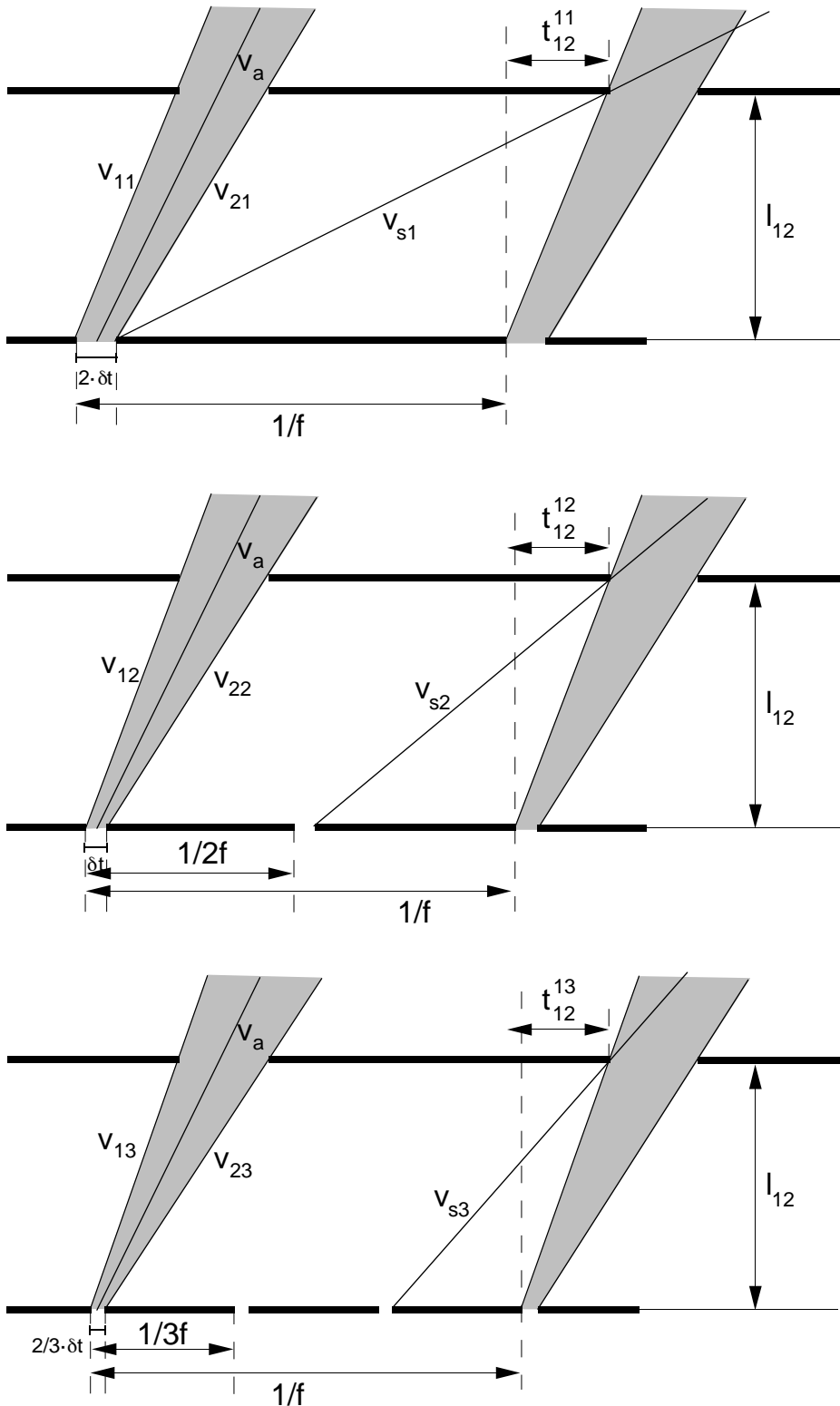


Fig. 11: Chopper 1 running at nominal frequency (top), at two times (middle) and three times the nominal frequency (bottom) and the snail chopper running always on nominal frequency. The threshold speeds v_{s1} , v_{s2} , and v_{s3} , respectively, are indicated.

A calculation for the instrument with $D = 3.2$ m (option c) is shown in Fig. 12. In practice a distance of 0.3 m should be sufficient to get rid of slow neutrons. Certainly for nominal-frequency measurements (50 Hz) there should not be any problem at all. In addition, the energies of such neutrons is much less than the analyzer energy, hence the neutrons have to gain energy at the sample in order to get counted. With low sample temperatures such scattering can be cancelled. The first - pulse producing - chopper will absorb the majority of neutrons and has to be able to run at much higher than the nominal speed (50 Hz). Since there exist some experience at SINQ and other sources of GdO_2 -coated carbon fiber composite disks withstanding high speeds and the radiation field produced by the neutron absorption, the pulse producing chopper is planned to be coated with GdO_2 . The disadvantage of Gd is its production of a large number of rather hard X-rays resulting in a large chopper shielding. In contrast, the slow moving choppers could be coated with boron carbide or ^{10}B with less severe gamma radiation field. The mechanical long-term properties of carbon fiber composites with such a coating is less well established but will not cause a problem at low speeds. In order to reduce the overall radiation at the first chopper pair an interchange of the first two choppers is planned. Hence, the first (snail) chopper (50 Hz, boron coated) will absorb about 99 % of the neutrons while at the second (pulse producing) chopper only a few tenth of a percent of the neutrons will be absorbed. The interchange can easily be realized since the equations above hold for this new arrangement as well.

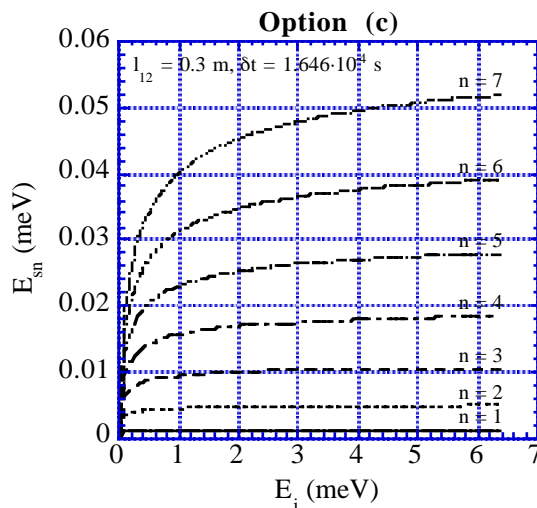


Fig. 12: Threshold energies as functions of incident energy for chopper speeds $f = n \cdot 50$ Hz

The rabbit chopper has to prevent a transmission of high energy neutrons originating from the next pulse (v_{r1} in Fig. 13) and - which turns out to be equivalent - to prevent slow neutrons (v_{r2} in Fig. 13) to pass through the chopper opening of the next pulse. The intersections of the time lines with the previous and next pulse, respectively, where these neutrons contaminate the useful energy window are marked by circles. Obviously this defines the maximum distance l_{13} between chopper 1 and the rabbit chopper as a function of the distance l_{12} . Since

$$v_1 = \frac{l_{12}}{2 \cdot \delta t} = \frac{L}{t_{1s}^1} \quad \text{and} \quad v_2 = \frac{L}{t_{1s}^1 + \Delta t - 2 \cdot \delta t} = \frac{l_{13}^{\max}}{1/f}$$

the maximum distance for the rabbit chopper turns out to be:

$$l_{13}^{\max} = \frac{L}{f \left[2 \cdot \delta t \cdot \left(\frac{L}{l_{12}} - 1 \right) + \Delta t \right]} \quad (2.13)$$

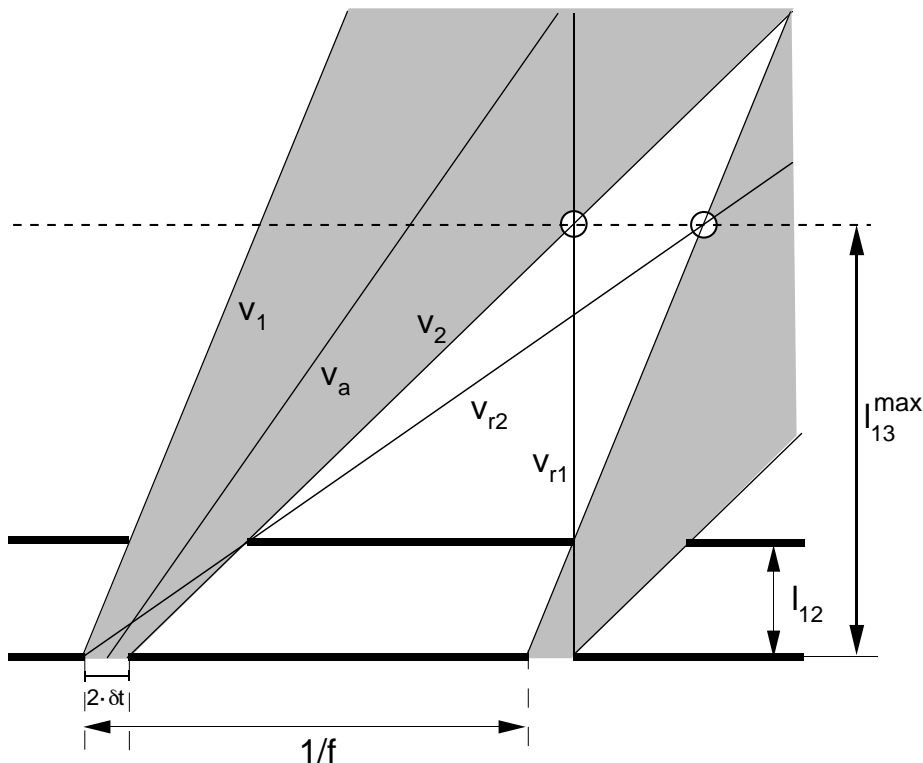


Fig. 13: d-t diagram of the first three choppers. The distance l_{13} of the rabbit chopper from the first chopper must not exceed the intersections marked by circles.

For $\Delta t = D/2 \cdot v_{002}$, $D = 3.2$ m, $\delta t = 1.646 \cdot 10^{-4}$ s, $f = 50$ Hz, $L = 38.6$ m, and $l_{12} = 0.3$ m eqs. 2.13 gives $l_{13}^{\max} = 15.8$ m as maximum distance between chopper 1 and 3.

As last condition for the primary instrument the non-overlap of preceding and following pulses with the actual pulse at the chopper pair 4/5 has to be assured (Fig. 14). Obviously:

$$\frac{2 \cdot \delta t}{l_{13}} = \frac{t_{4o}}{L - l_{13}}. \quad (2.14)$$

With the above values this results in $t_{4o} = 1.574 \cdot 10^{-3}$ s compared to $\Delta t = 7.520 \cdot 10^{-3}$ s and $t_{4c} = 11.279 \cdot 10^{-3}$ s ($= (1/f) - \Delta t$). Clearly there is no danger of an overlap at the last choppers (the same is true for the other configurations (a) and (b) and even more for the mode with higher chopper 1 speeds).

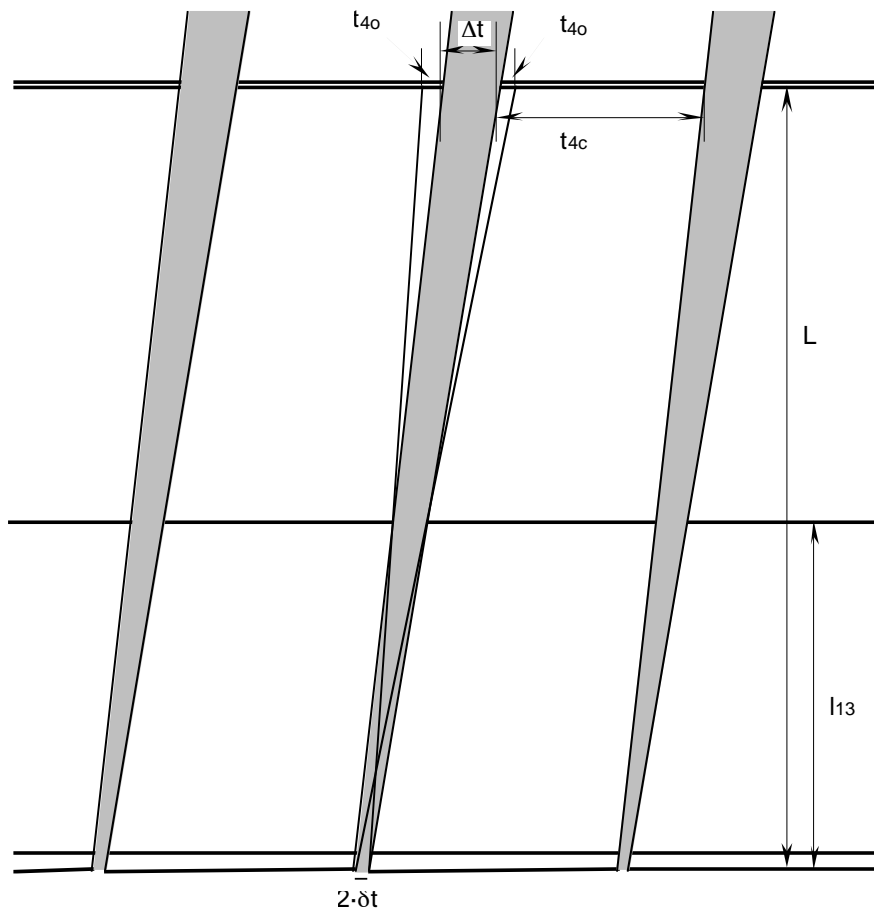


Fig. 14: d-t diagram of the whole primary instrument with illumination time at chopper 4/5.

3.5 Energy resolution in the primary instrument

For the instrument developed in the previous chapters the primary energy resolution is given by reformulating eq. 2.10. In Fig. 15 the resolution is plotted as function of incident energy with the values of option (c) [$D = 3.2$ m, $L = 38.6$ m, $d_b = 1.5$ cm, $r_b = 29$ cm].

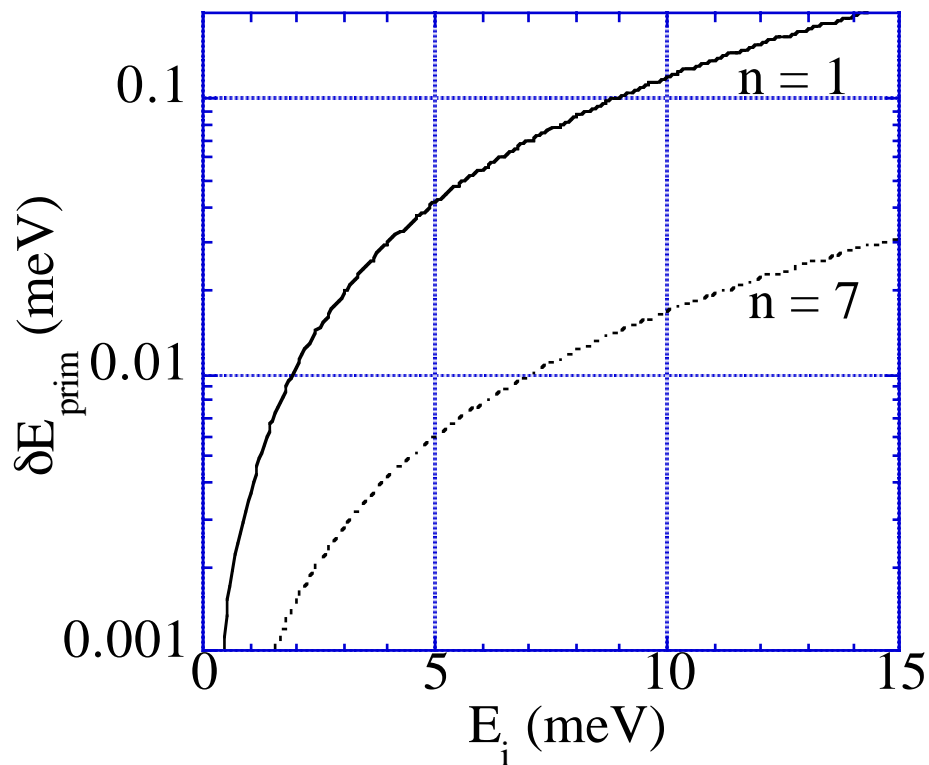


Fig. 15: Energy resolution in the primary instrument for the two extreme chopper frequencies of option c.

4. Energy Analysis

4.1 Principal layout

As was already mentioned in Chapter 2 for an inverted TOF instrument an off-backscattering geometry has to be chosen if inelastic processes take place in the sample. The reason for this is shown in Fig. 16: In a conventional backscattering instrument a part of the neutrons scattered from the sample are backscattered at the analyzer bank, pass the sample a second time and are finally absorbed in the detector (sketch A in Fig. 16). An other part of the neutrons will hit the detector right after being scattered at the sample. If the scattering processes were purely elastic the flight path of a neutron could be reconstructed with the help of a time sensitive detector. As soon as inelastic scattering processes may take place in the sample this is not possible as can be seen in Fig. 16 (top): Two neutrons scattered at the sample ((1)) reach the detector at the same time ((2) and (3)), but while one was scattered in the mean time at the analyzer the other with its lower energy just flies to the detector during the same time. Hence, the energy information gets lost. In order to avoid the possibility of two different flight paths one has to build the instrument in slight off-backscattering geometry with a shielded detector (Fig. 16, sketch B). In this arrangement only neutrons scattered at the sample and the analyzer will finally reach the detector.

4.2 Secondary energy resolution

The disadvantage of an off-backscattering geometry is its lower resolution compared to the perfect backscattering geometry as can be seen by differentiating Bragg's law by d (scattering plane spacing) and Θ :

$$\frac{\delta\lambda}{\lambda} = \frac{\delta d}{d} + \text{ctg}\theta \cdot \delta\theta. \quad (3.1)$$

For $\Theta = \pi/2$ and perfect analyzer crystals theoretically $\delta\lambda/\lambda$ goes to zero, but in practice - due to finite sample and detector size - slightly smaller angles appear even in the perfect backscattering geometry (A). In such a case not $\pi/2$ but the mean value ($\pi/2 - \delta\Theta$) of the occurring angles have to be taken for Θ . In the off-backscattering geometry smaller analyzers (in vertical

direction) have to be chosen in order to preserve good resolution by minimizing $\delta\theta$.

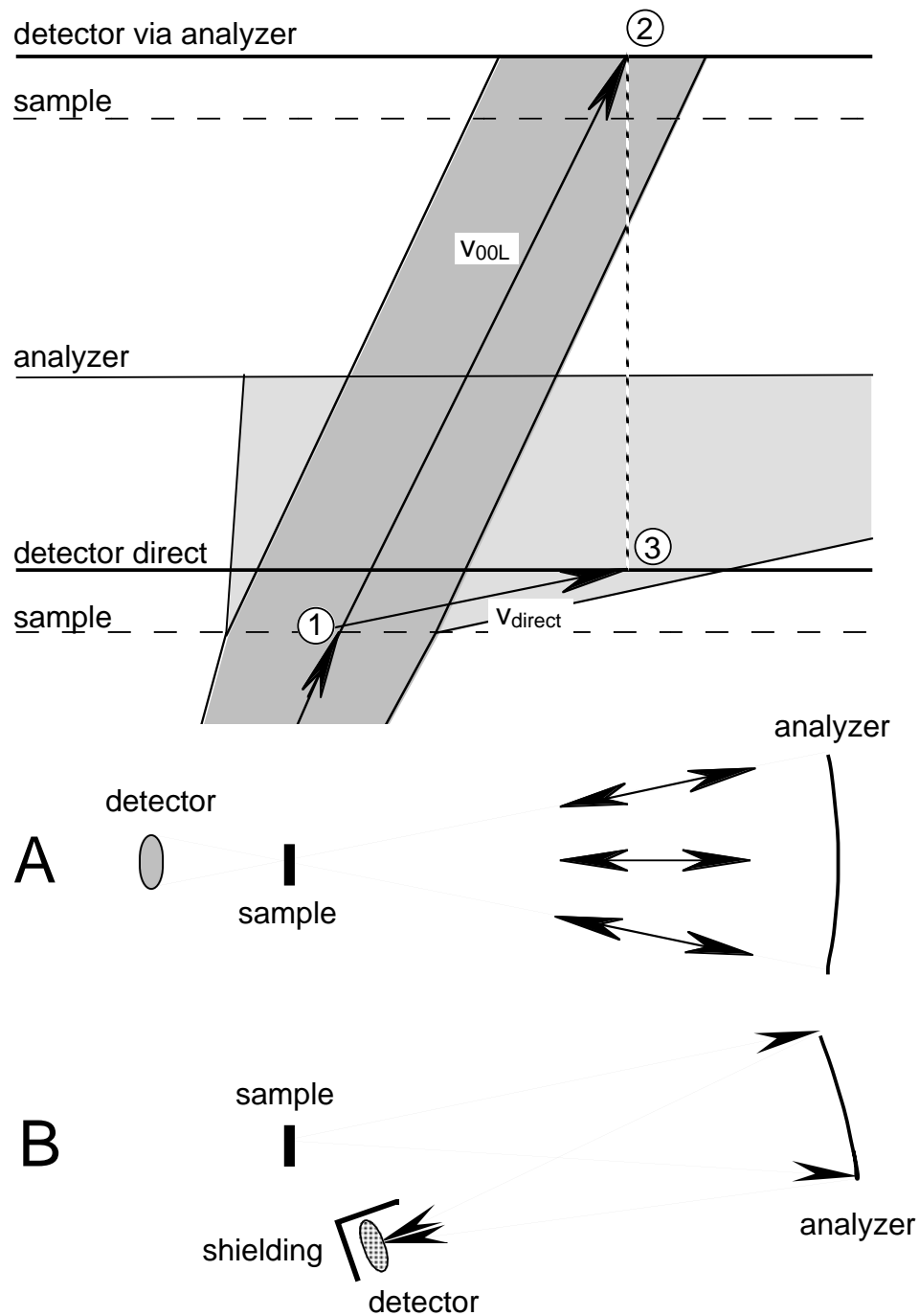


Fig. 16: d-t diagram of the secondary instrument and the two principal instrument layouts: Perfect backscattering geometry (A) and off-backscattering geometry (B).

For perfect analyzer crystals the accepted angular divergency is not $\delta\Theta$ for each point of the analyzer. $\delta\Theta$ for such crystals is just the angular spread over the whole analyzer as can be seen in the exaggerated diagram in Fig. 17.

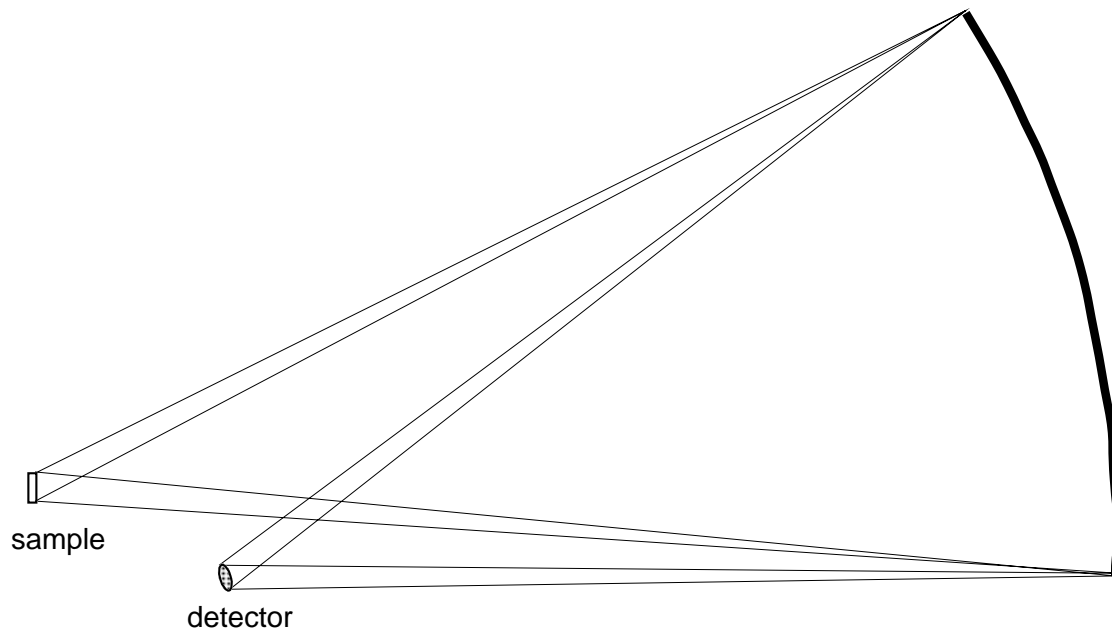


Fig. 17: Exaggerated view of the off-backscattering geometry. The variation of angles is distributed over the whole analyzer: Maximum angle is 88.4° (bottom), average angle 86.2° , and minimum angle 84.1° (at the top).

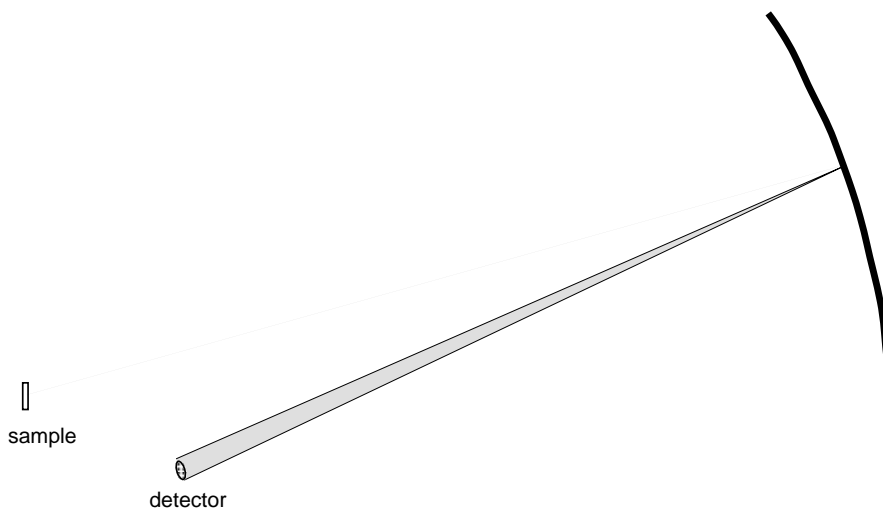


Fig. 18: The mirror image of a point on the sample is distributed over the whole detector if the mosaicity of the analyzer crystal matches the beam divergency at the analyzer. The intensity is increased compared to a point to point projection.

Each point on the sample has exactly one mirror image at the counter. Hence, the relatively large Θ and $\delta\Theta$ lead according to eq. 3.1 to a bad resolution, but this is not rewarded with a higher intensity. In order to increase the intensity (without worsening the resolution remarkably) the mosaicity η of the analyzer crystal has to be adjusted to the beam divergency α at the analyzer (Fig. 18 and Fig. 19).

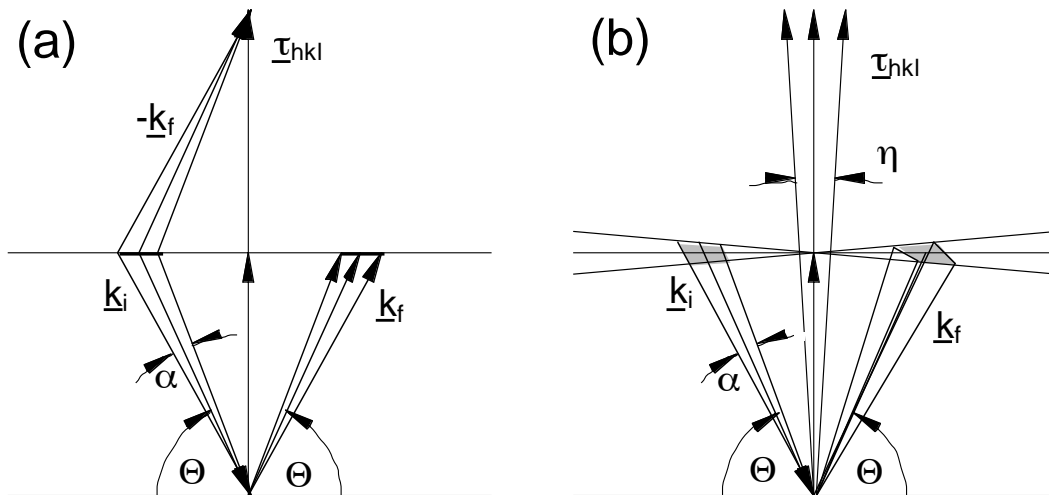


Fig. 19: Phase-space transformation for a perfect crystal and diverging beam (a) and a crystal with mosaic spread η and beam divergency α (b). The dashed area in (b) corresponds to the reflected intensity. In (a) this area collapses into a line and hence an almost zero intensity.

The wave vector uncertainty δk due to divergency and mosaic spread is given by:

$$\delta k = k \cdot \text{ctg}\Theta \cdot \sqrt{\alpha^2 + \eta^2}. \quad (3.2)$$

With $\delta k/k = \delta E/2E$ and

$$k = \frac{\sqrt{81.81 / 2.072}}{2d_{00l} \sin \theta}. \quad (3.3)$$

this results in:

$$\delta E = \frac{81.81}{2} \frac{\cos \theta}{d_{00l}^2 \sin^3 \theta} \sqrt{\alpha^2 + \eta^2}. \quad (3.4)$$

The resulting energy resolution and the relative intensity (dashed area in Fig. 19 b) as a function of mosaic spread η and beam divergency α for a fixed value of Θ are displayed in Fig. 20. Since the values for the intensity and resolution are symmetric in α and η the optimal combination is realized for $\alpha = \eta$.

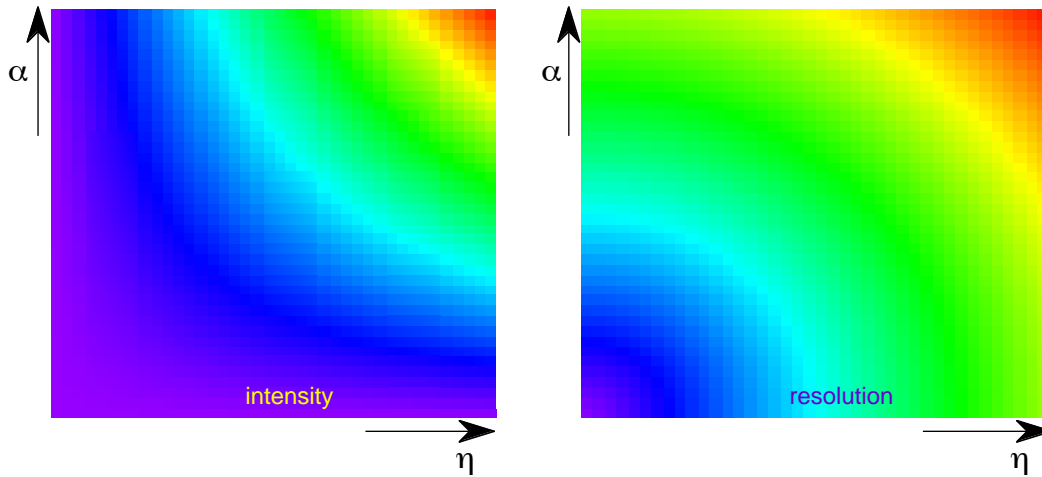


Fig. 20: Relative intensity (left) and resolution (right) as a function of mosaic spread η and divergency α . (Small values in purple and large values in orange.)

Combining eq. 3.1 and 3.2 under the assumption of a Gaussian distribution (neglecting $\delta d/d$) leads with $\delta\lambda/\lambda = \delta k/k$ to a total k-uncertainty of:

$$\delta k_{tot} = k \cdot \text{ctg} \theta \cdot \sqrt{(\delta\theta)^2 + \alpha^2 + \eta^2} \quad (3.5)$$

and finally to a energy resolution in the secondary instrument of:

$$\delta E_{sec} = 2E \cdot \text{ctg} \theta \cdot \sqrt{(\delta\theta)^2 + \alpha^2 + \eta^2}. \quad (3.6)$$

Up to now we did only care for the vertical part of the scattered and analyzed beam. The horizontal part is much more symmetric than the vertical

part (Fig. 21) and hence $\delta\Theta$ is very small and Θ almost 90° in the horizontal plane. The angle of the sector covered with analyzers can additionally be decreased by putting more analyzer banks and accordingly more detectors in the instrument. Furthermore, due to the smaller sample and counter dimensions in this plane the beam divergency α becomes smaller compared to the vertical arrangement. Due to these reasons the horizontal arrangement is - within certain limits - not resolution limiting.

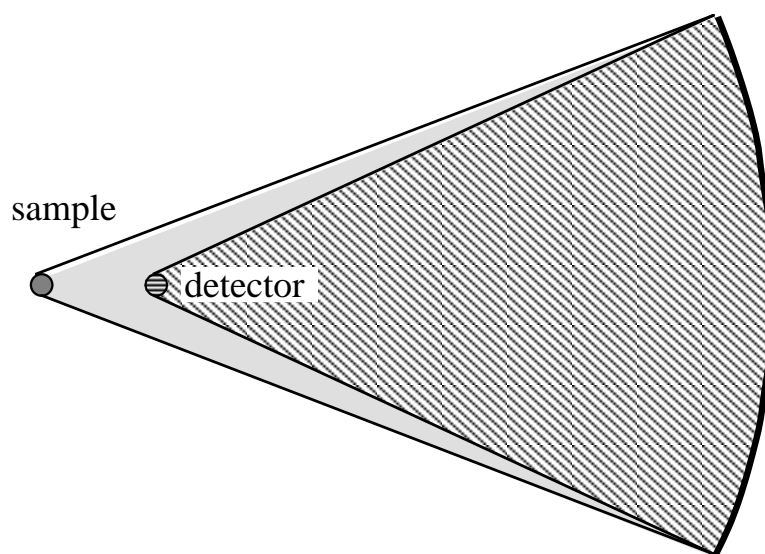


Fig. 21: Horizontal view of a analyzer bank with sample and detector. Note the more symmetric arrangement compared to the vertical geometry displayed in Fig. 17.

In conclusion, the secondary energy resolution is primarily defined by $\delta\Theta$, since the divergency α (defined by the distance between sample and analyzer and the sample size: For option c typically 0.5° [FWHM]) and the mosaic spread η (for mica: 0.55 - 0.65°) are - once chosen - fix. For $\alpha = 0.5^\circ$ ($8.7 \cdot 10^{-3}$ rad) and η of the same size $\delta\Theta$ can be as large as 1.7° ($3.0 \cdot 10^{-2}$ rad) (with option c, $\delta E_{\text{sec}} = 0.707 \mu\text{eV}$, $E = 0.208 \text{ meV}$, $\Theta = 87^\circ$). This can be realized by an analyzer bank of 36° inclined (vertically) by 30° . Such a bank extending as a zone around the sample would cover typically on forth of the corresponding sphere. In practice, due to restriction in the direct beam direction and shielding, a coverage of typically $1/8$ of the sphere surface is feasible. In order to increase this area a second bank could be installed (Fig. 22 and 23).

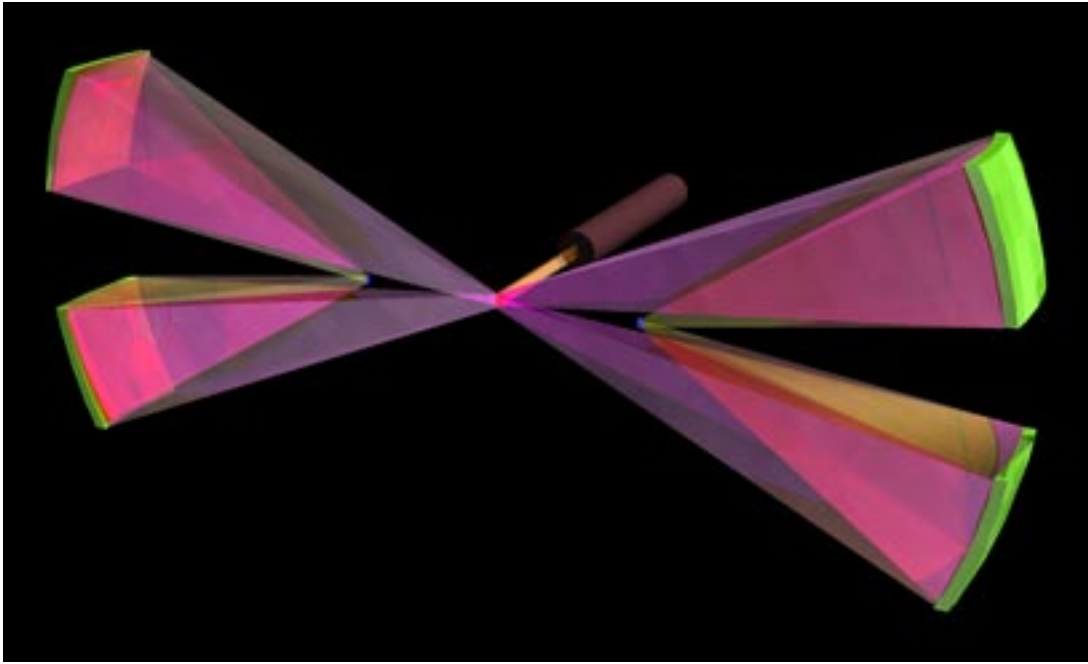


Fig. 22: Pairs of analyzer banks (90° banks) sharing one detector.

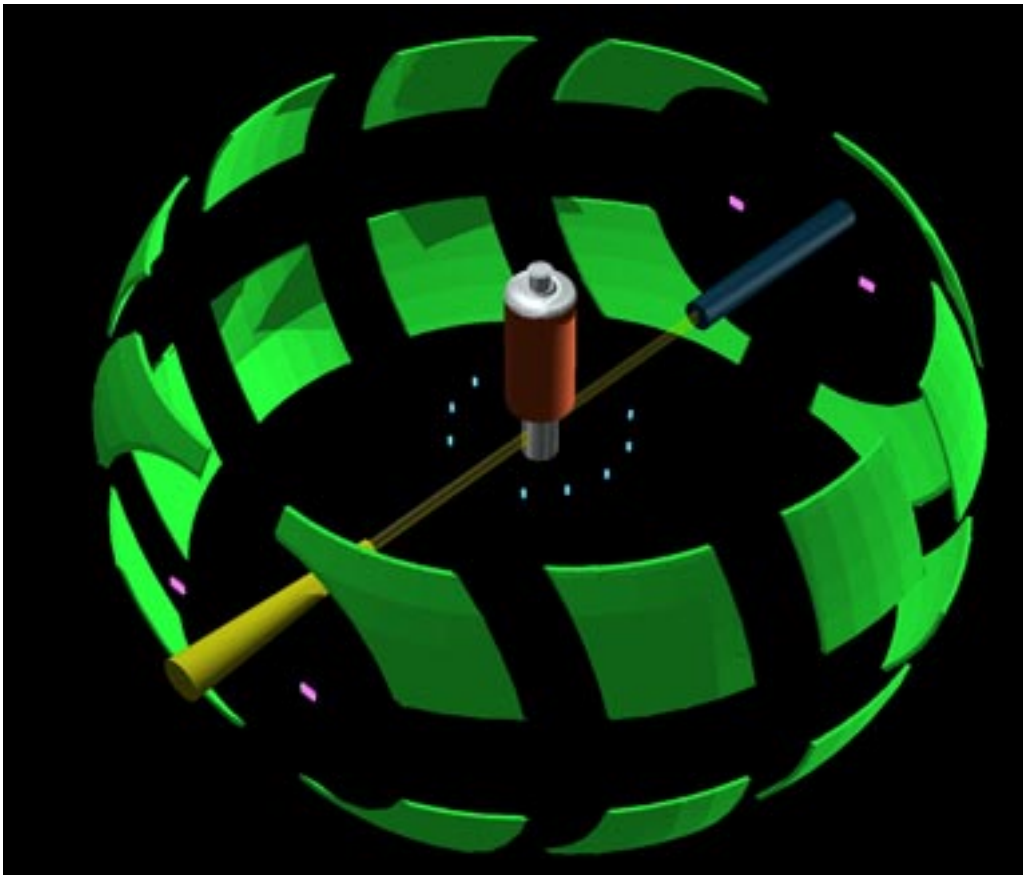


Fig. 23: View of all analyzer banks. They are the intersection of Debye-Scherrer cones with the sphere zones. (Pink: diffraction detectors.)

These two banks can be arranged in such a way that only one detector is needed (per bank pair). This slightly increases the path length uncertainty δl (less than 1 cm in option c).

4.3 Mobile analyzer banks

Now we finally have an equilibrium energy resolution for the primary and the secondary instrument for an incident energy which corresponds to the analyzed energy of the mica 00L reflection (i.e. 0.208 meV). This total resolution of 1 μeV worsens if the incident energy increases, but only due to a worsening of the resolution in the primary instrument. The resolution of the secondary instrument remains at its value of 0.707 μeV . Hence, there is no resolution mapping anymore at higher incident energy and the neutron intensity at the detectors is smaller than theoretically possible. In order to overcome this limitation the resolution of the secondary instrument has to be worsened simultaneously with that of the primary instrument. This can be done by decreasing the scattering angle Θ (Fig. 24). The corresponding gain in intensity is displayed in Fig. 25. With movable analyzers and detectors the bank-pair arrangement shown in Fig. 22 and 23 is not possible anymore. Therefore, such a set-up decreases intensity at low incident energies (and high resolution) but increases intensity at high incident energies (break-even is at around $\Theta = 81^\circ$).

For optimal results the analyzer banks have to be adjusted to the incident energy and the mica reflection used for the measurement. This dependence is shown in Fig. 26.

The disadvantage of this variable scattering angles is the variation in the analyzer penetration depth of the neutrons: small (about 1 mm) for backscattering and large (about 7 mm) for $\Theta = 50^\circ$. In order to profit from the intensity gain depicted in Fig. 25 the analyzers have to be thick (5-7 mm) which will increase the background to signal ratio in the small- Θ positions. Alternative mica crystals (phlogopite) will reduce this background to an acceptable level.

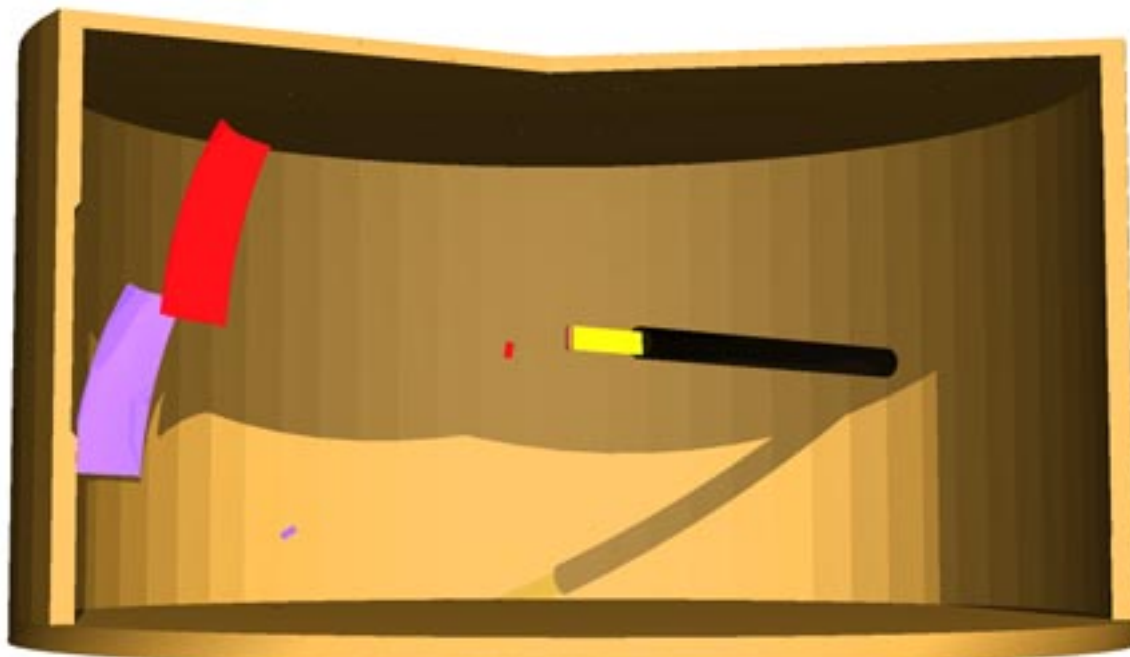


Fig. 24: Movable analyzer bank and detector. High- Θ arrangement (red) and low- Θ arrangement (purple).

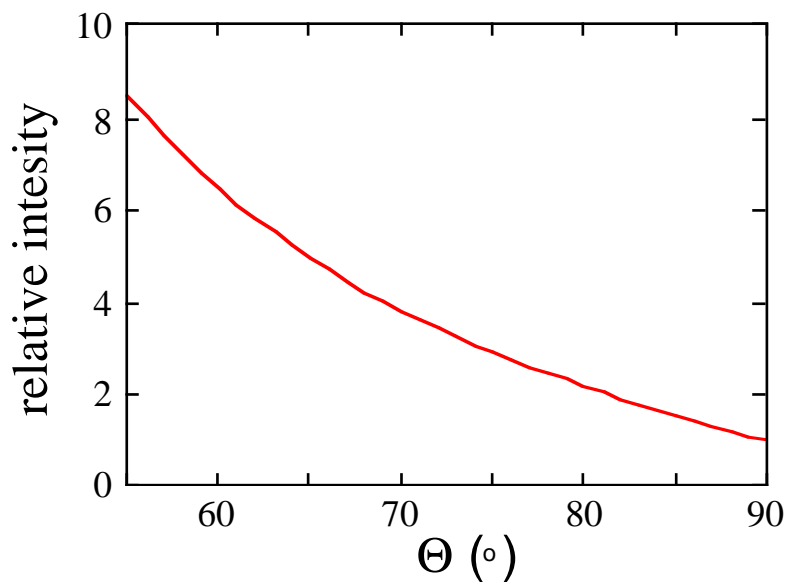


Fig. 25: Relative intensity as a function of "backscattering" angle Θ (normed to 90°)

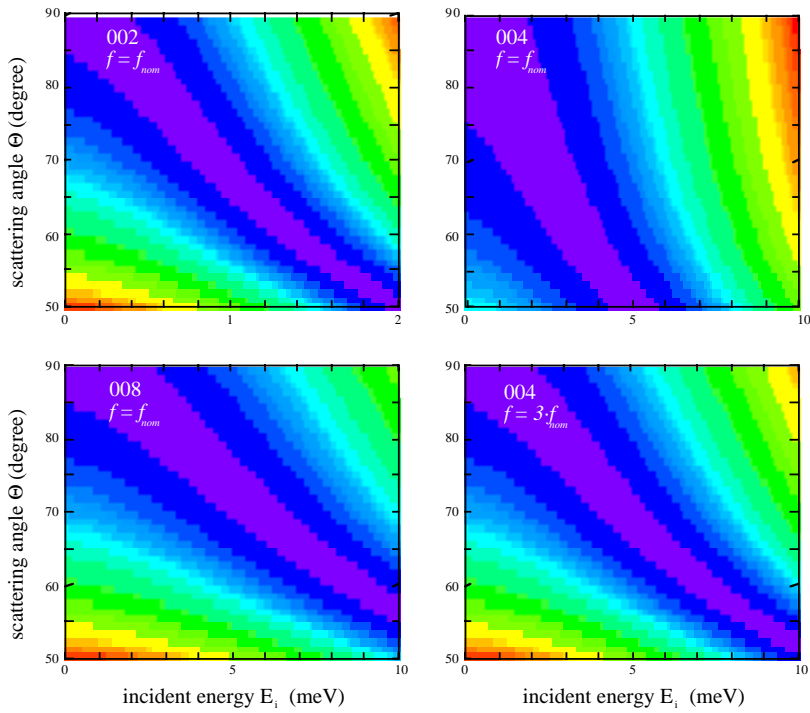


Fig. 26: The purple regions indicate matching primary (see Fig. 15) and secondary energy resolution for different incident energies, scattering angles, mica reflections, and chopper frequencies.

5. Instrument data

5.1 Energy resolution and energy windows

The worsening of the resolution for the instrument with movable analyzers is relatively small, and - if necessary - the analyzer banks in an instrument with movable banks can be kept fix at the maximum angle (but with a intensity penalty of a factor of two due to the total analyzer area).

The total energy resolution for different setups is shown in Fig. 27 for an instrument with movable analyzer banks. The total energy window (which is essentially independent of the layout of the secondary instrument) is also shown in Fig. 27.

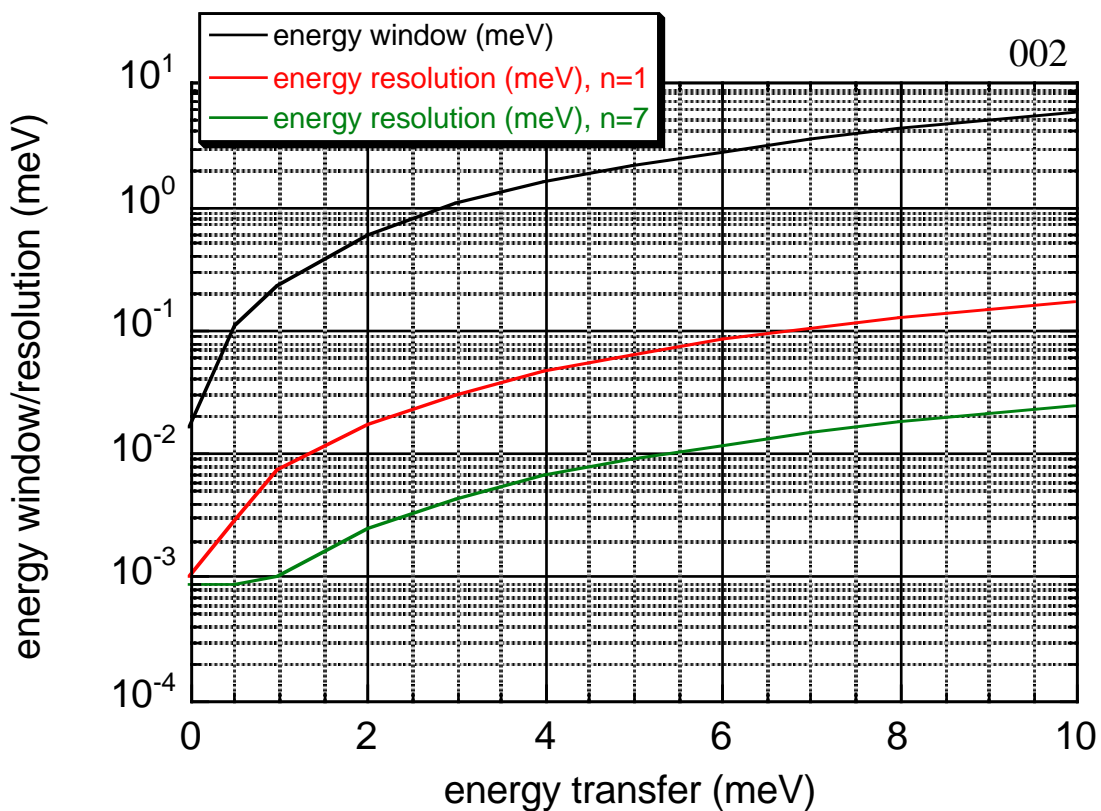


Fig. 27: Total energy resolution and energy window for an instrument with mobile analyzer banks.

5.2 Q-ranges

Under the assumption of analyzer banks spanning from 30 to 150 degrees the resulting Q-values - depending on the chosen reflection and the incident energy - cover the range between 0.16 and 3.7 \AA^{-1} (Fig. 28).

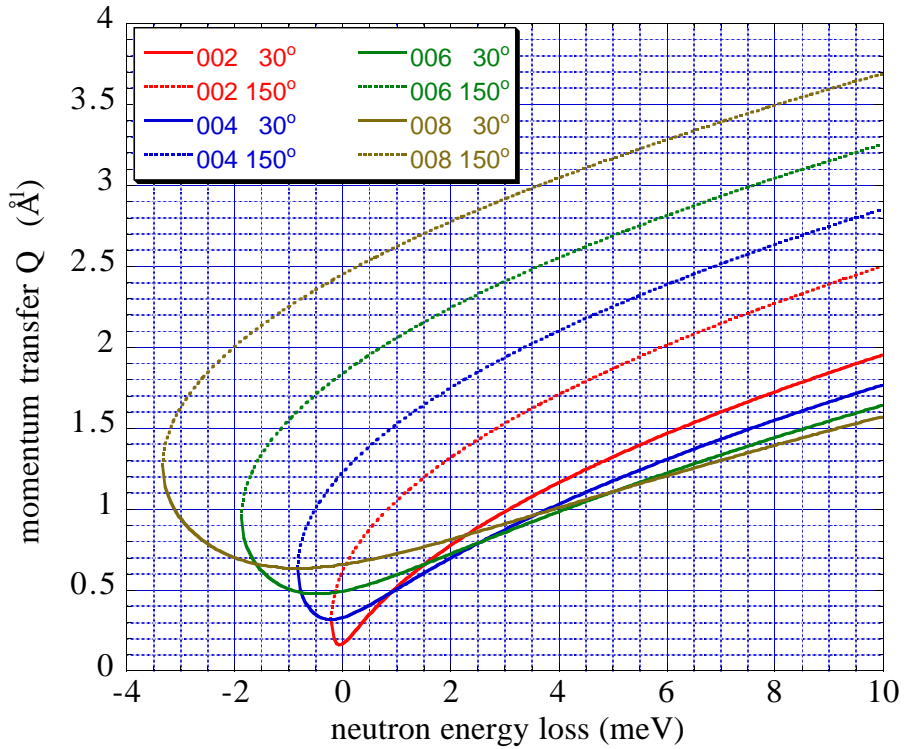


Fig. 28: Moduli of the scattering vector as a function of energy transfer, analyzer reflection, and analyzer angle. The obtainable values for a given reflection lie between the solid and the dashed line of the corresponding color.

5.3 Intensity

For all the following calculations a current of 1 mA and a Pb-target was assumed for SINQ.

Let us first compare the number of available protons/pulse at ISIS with that of SINQ (taking into account only these protons which provide neutrons during the chopper opening time window). The number of protons/pulse at ISIS is $2.5 \cdot 10^{13}$. At SINQ with 1 mA current and $0.16 \cdot 10^{-3}$ s chopper-1 opening time δt a total charge of $0.16 \cdot 10^{-6}$ C hits the target during this time. These corresponds to $8.5 \cdot 10^{11}$ protons/pulse or 29 times less than at ISIS. A gain factor of two compared to ISIS is expected for SINQ because of a better positioning of the cold source. Another factor of two is gained with the larger guide cross section. The consequent usage of supermirror coated neutron guides at SINQ results in another factor of three. The calculated neutron flux at the sample in the chopped beam for MARS and the measured flux for IRIS (D. Martin, S. Campbell, and C.J. Carlile) is shown in Fig. 29. The flux and hence the intensity (since the sample size is about the same in both instruments) is not more than a factor 2 less for MARS compared to IRIS.

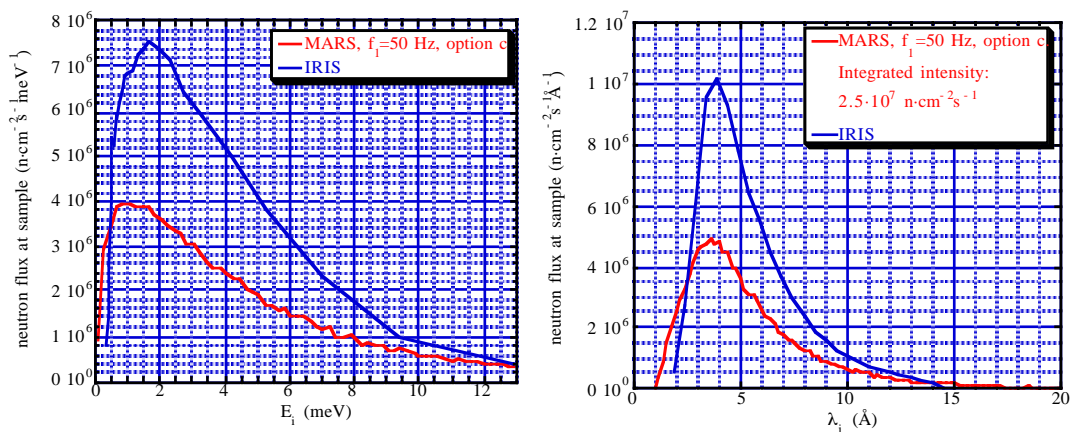


Fig. 29: Neutron flux for MARS (calculated) and IRIS (measured) as a function of incident wavelength (left) and incident energy (right).

In IRIS only one side of the sample is covered with mica analyzers while the other side consists of graphite analyzers. Therefore, an equipment with mica analyzers on both sides (as planned for MARS) will result in an identical final intensity in both instruments. But the analyzer banks for

MARS are larger than the ones in IRIS by a factor of about 3 and the mica used (phlogopite) will scatter about 5 times better, hence MARS should be a very competitive instrument.

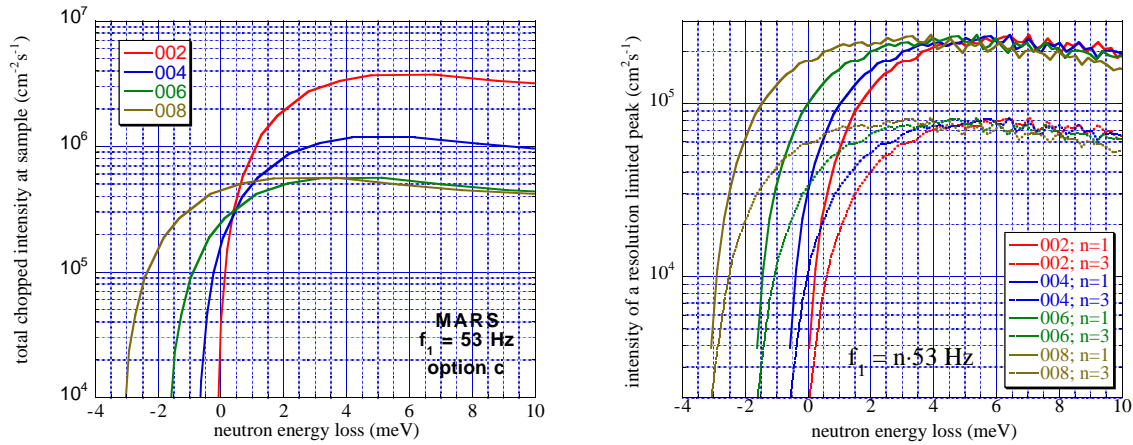


Fig. 30: Total energy window dependent number of neutrons reaching the sample (left) and primary intensity of a resolution limited peak (right).

Since IRIS and MARS have a very similar instrument layout (primary pathlength, pulse frequency) the following points will apply not only to MARS but to IRIS as well:

The neutron flux shown in Fig. 29 is the flux expected if only the first chopper is running (IRIS: pulse out of moderator) and all the other choppers are in an open position during the whole time. In practise these additional chopper will cut only a small (incident energy depending) part out of the neutron spectrum (see Fig. 27). Hence, the flux in Fig. 29 has to be multiplied by the energy window in order to obtain the number of neutrons arriving at the sample (Fig. 30, left). The left side of Fig. 30 mirrors essentially the fact that for a large energy window more neutrons will reach the sample than for a small energy window. This is not a very useful information for an experiment planning. Let us therefore assume that there are several resolution limited peaks (i.e. $< 1 \mu\text{eV}$) of identical strength distributed in the whole accessible energy transfer range. Then the number of neutrons with proper incident energy is given by the flux (as a function of energy transfer) times the energy resolution (Fig. 30, right). If the peaks have an intrinsic width which is larger than the resolution then the intensity is just this energy width times the flux shown in Fig. 29.

The final intensity of the instrument will scale with the relative intensity of the different muscovite mica reflections 00L. These values relative to 006 and measured at the corresponding elastic peak positions are (pyrolytic graphite PG002 would be 2.5 in this scale):

	<u>002</u>	<u>004</u>	<u>006</u>	<u>008</u>
LAM-80, Tsukuba, Japan	0.091	0.465	1	0.395
IRIS, ISIS, UK	0.1	0.6	1	?

Since the flux distribution of IRIS and MARS are comparable (with light relative advantages at high and low energies for MARS), the relative intensities on MARS will be comparable to the values for IRIS given above if equipped with muscovite. Equipped with phlogopite the relative intensities are similar but the absolute intensity a factor of 4 to 6 higher (Fig. 31)

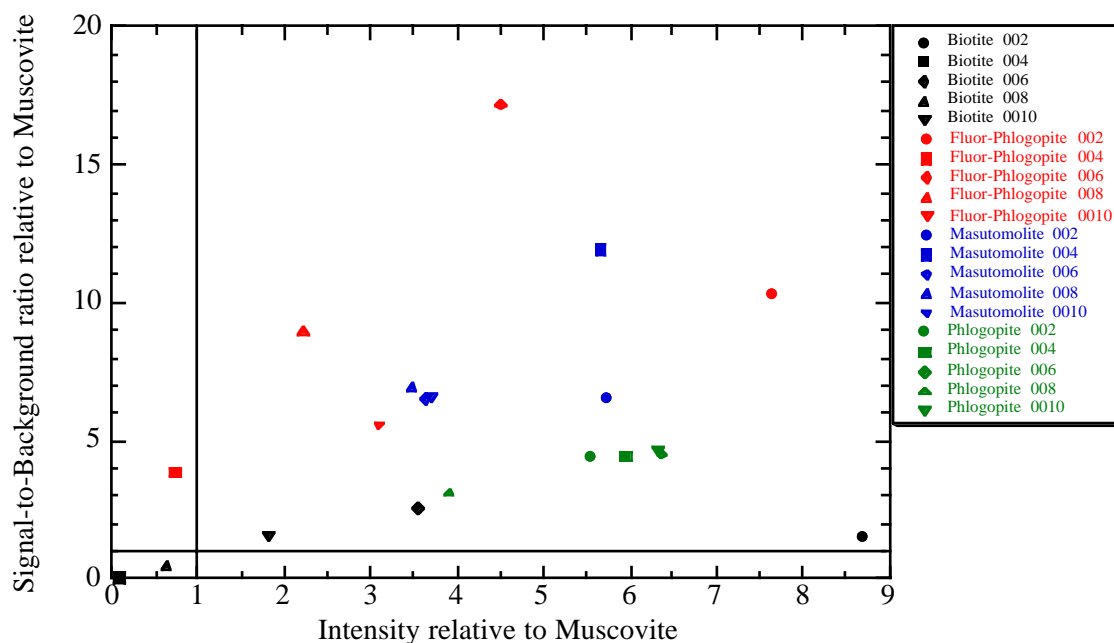


Fig. 31: Comparison of the intensity of some micas (relative to muscovite)

Let us now compare the flux for a conventional backscattering instrument (BS) with that of MARS. The first chopper of MARS is only open for about 1/120 of the time (chopper window: 3°). This decreases the flux from the source by this factor (see Fig. 32: flux from source in red and chopped flux in blue). As described above only a part of the neutron are transmitted through the following choppers, resulting in an (incident energy

dependent) energy window. The final neutron flux arriving at the sample corresponds therefore to the blue area in Fig. 32. A BS cuts with its monochromator only a small part out of the incident flux. Since such an instrument needs a chopper in order to discriminate neutrons which directly hit the detector from the ones which travel all the way to the analyzer and back to the detector, the actual flux at the sample is about one third (120° chopper window) of the cut out flux (green column in Fig. 32). Hence, for a given time the intensity at a defined energy is 20 times higher in the BS, but in the same time MARS counts neutrons in the whole energy window. If therefore twenty measurement points in the BS are needed to obtain a reasonable spectrum the intensities are equal, but with more points MARS is superior.

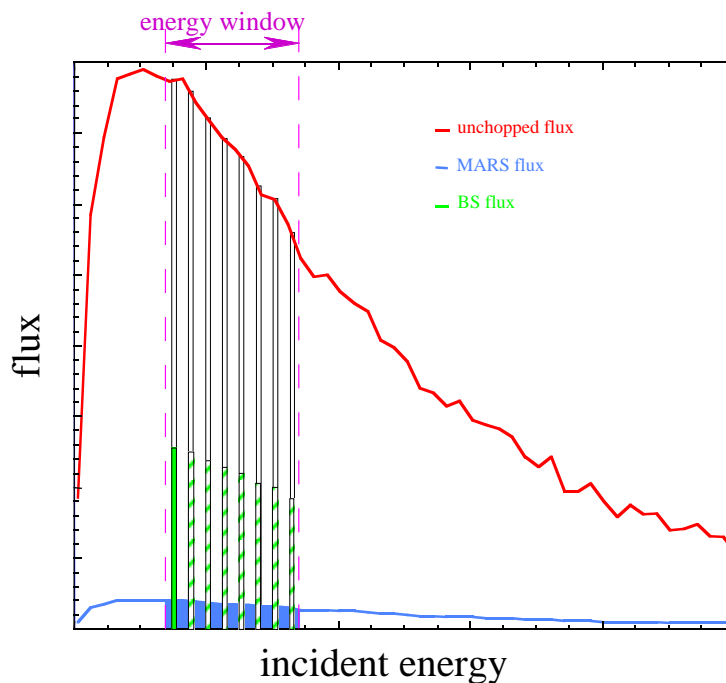


Fig. 32: Schematic plot of the unchopped flux (red curve), flux in MARS (blue area), and flux in a backscattering instrument (green area). The flux in MARS is actually exaggerated by a factor of three for clarity.

But the advantage of a TOF instrument is - independent of intensity (if the difference to a BS is not too large) - its flexibility in choosing the incident energy and the fact that after a short measurement time data in the whole energy window can be visualized and depending on the result the

measurement can be continued or stopped. This means an essential time conservation in comparison with a BS, where almost the whole scan has to be completed before a decision about the usefulness of the spectrum can be made.

5.4 Polarization analysis

Since the number of detectors is limited to typically six on each side (plus the diffraction detectors, see below) polarization units can be installed in front of them. In order to decrease the complexity and the expenditure of installations these polarizers are planned to be remanent (supermirrors with a magnetic field supplied by permanent magnets installed in the polarizer casing). Hence, a flipping of polarization is not possible in these polarizers. A polarizer in front of the sample with the option to flip the polarization will enable us to distinguish non-spin flip from spin flip scattering. The guide field within the instrument will be generated by two Helmholtz coils installed at the top and bottom of the instrument casing.

5.5 Diffraction

Since the incident beam consists of a band of energies MARS can as well be used to measure in a diffraction mode if some TOF detectors are installed at about the same distance from the sample as the analyzer banks. Here the neutrons directly hitting the detectors after having been scattered at the samples are counted. In the normal mode the resulting d-spacing window is very small but can easily be adjusted to a wished value by changing the incident energy (Fig. 33). For a control of phase transitions due to temperature, pressure, etc. this should be sufficient. If a larger range is needed the choppers 2 to 5 can be run at a i -times lower frequency (with an intensity penalty of i -times less intensity) or these choppers can be stopped in the open position. The resolution $\delta d/d$ which is independent of the d -range is given in Fig. 34. A n -times higher pulse-chopper frequency increases the resolution by a factor of n without affecting the d -range.

With the present design of relatively few analyzer banks (6 on each side) all the positions between the banks can be used for diffraction

detectors. This will lead to a complete coverage of d-spacing between the extreme values depicted in Fig. 33.

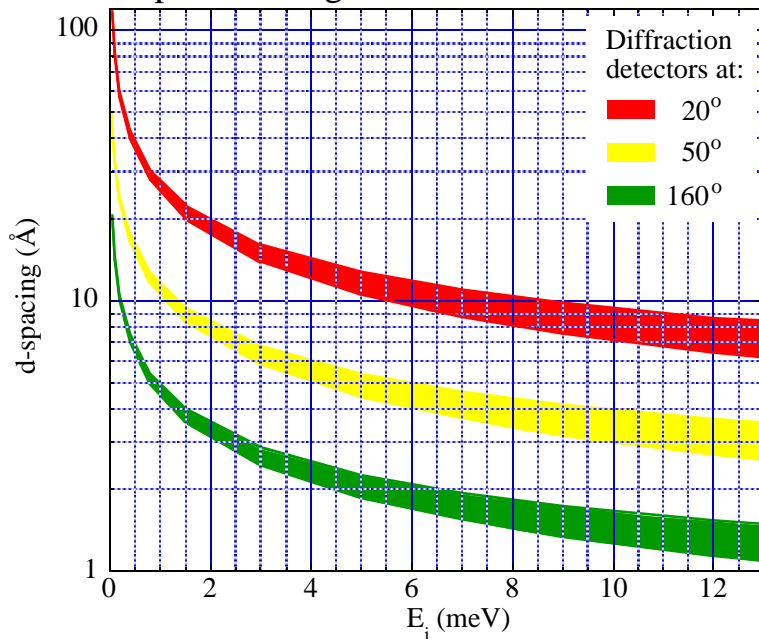


Fig. 33: Accessible d-spacing in normal mode operation (50 Hz except for the pulse producing chopper)

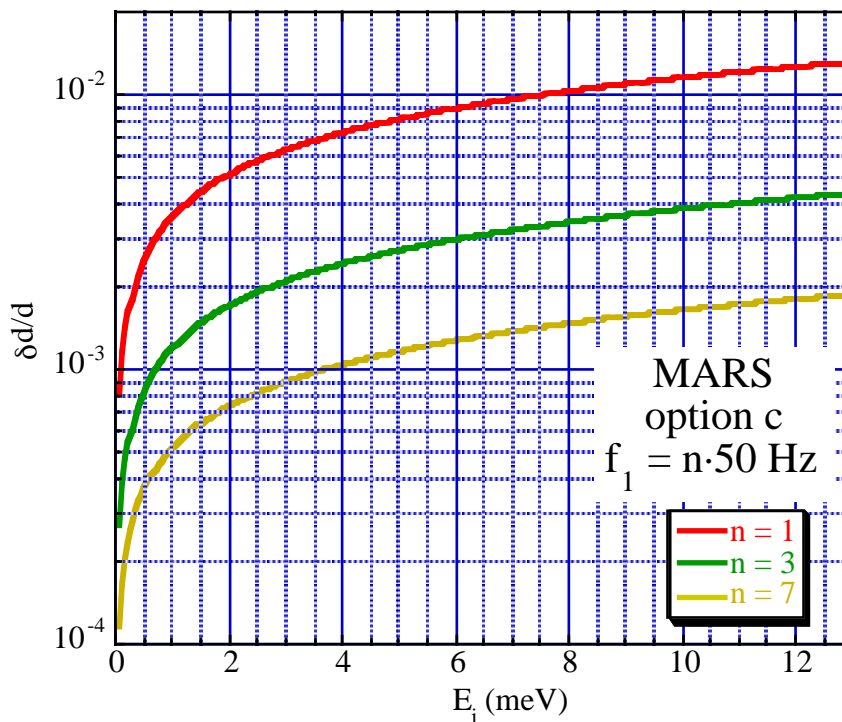


Fig. 34: Resolution $\delta d/d$ as a function of incident energy for the pulse-chopper frequencies 50, 150, and 350 Hz.

5.6 Costs

Estimated costs of the instrument with mobile analyzers (in Swiss francs):

choppers (5) including electronics:	1'100'000
chopper shielding	240'000
instrument casting and shielding:	700'000
mica analyzer (4 m ²):	50'000
analyzer mechanics and electronics:	200'000
TOF counters (22) and electronics:	120'000
Be filter:	<u>60'000</u>
total costs:	2'470'000
neutron guide extension	710'000

6. Conclusion

Since there are some instruments available at different sources for quasi elastic and slightly inelastic research, an instrument for inelastic investigation and high resolution would be welcomed more. In addition, on IRIS most of the measurements are done with the graphite analyzers or mica 004-, 006-reflections and not with mica 002. At the best "backscattering" position for the presented instrument the scattering angle is about 87° and therefore already quite close to the break-even point at 81° (see Fig. 25). Therefore, the instrument should be equipped with mobile analyzers

The proposed instrument is an inverted TOF machine with five choppers running with 50 Hz (350 Hz option for the pulse chopper) and a secondary instrument with movable banks of mica analyzers on both sides of the instrument. A total length of the primary instrument of 38.6 m and a diameter of 3.2 m for the secondary instrument (without shielding).